Master thesis | Mathematics section

Biomechanical model of the primates' upper limb: design of stimulation protocols for the recovery of reaching movements in tetraplegia

Pierre Kibleur

Professor:	Auke Ijspeert (EPFL)
Principal investigator:	Marco Caprogrosso (UniFr)
Supervisors:	Nathan Greiner
	Shravan Tata Ramalingasetty

September 19th, 2017
-
January 19th, 2018

This page intentionally left blank.

Abstract

Recent advances in neuroscience led to the development of therapies for paraplegic patients, currently at the stage of clinical trials, that permit to some extent the restoration of the patients' natural control over their lower limbs through the electrical stimulation of the sensorial input to their spinal cord. Faced with the individual's benefits of such therapies, future developments will focus on porting the technology to the upper limbs, thus bringing partial solutions for increasing the quality of life in tetraplegia.

Beyond evident anatomical similarities, the primates are the only animals sharing the direct cortico-motoneuronal pathway with humans, making their study necessary to develop strategies of spinal cord stimulation. Throughout this thesis, a computational model of the primate's arm is developed on the OpenSim platform from a previously published but now obsolete SIMM model. Skeletal and muscular morphometric data is gathered, adapted and added until the model is validated dynamically, and its ability to reproduce the real animal's experimental motion in a closed loop is asserted. The model is then used to predict, in the spinal cord, the spatiotemporal patterns of neuronal activation underlying the subject's motor behaviour during a stereotypical reaching and grasping task. An estimation of the afferent fibres' firing rates will be critical to the understanding of the interactions between the stimulation and the neuronal circuitry, and will alleviate challenges faced in recording the normal sensorimotor activity in real time. As such, the model lays some foundations for the development of future therapies.

This page intentionally left blank.

Contents

Chapter 1 Introduction

1.1 Motivation

A human's ability to control his limbs is lost as soon as the physical link between the brain and the limb's actuators, the muscles, is broken. A spinal cord injury can be the cause of such a rupture, after only the fraction of a second it takes for an accident to occur.
But what if the Central Nervous System's (CNS: comprised of both the brain and the spinal cord) control of the limbs was understood well enough that human technology could take over, when the communication between the brain and the muscles is interrupted? In the early 1960's already, the first recordings of individual neurons' activity during motor behaviour were made in awake, healthy animals [1], opening the path for the study of neuromusculoskeletal models aiming at learning the natural control of the limbs. More recent advances showed that it is possible to restore a Non Human Primate's (NHP) ability to walk after a spinal cord injury [2], advances which are now being converted into a therapy for humans [3].
Furthering this progress, we believe that it will eventually be possible to restore the control over the upper limbs as well.

1.2 Framework and objectives

As much as restoring the normal walking gait has been the primary focus of the lower limbs studies, restoring the ability to reach is a priority in studies of the upper limbs. Indeed, the action of reaching is ideal for neuromusculoskeletal modelling, as it involves strong activation levels of a large amount of neurons [4], as well as the actuation of all the principal Degrees of Freedom (DoF) in a primate's arm. To produce a reaching movement, the healthy subject's CNS converts a target location in space into a set of muscle commands. It is generally agreed that this transformation can be coherently divided into a set of discrete steps [5] as schematized in Figure 1.1.

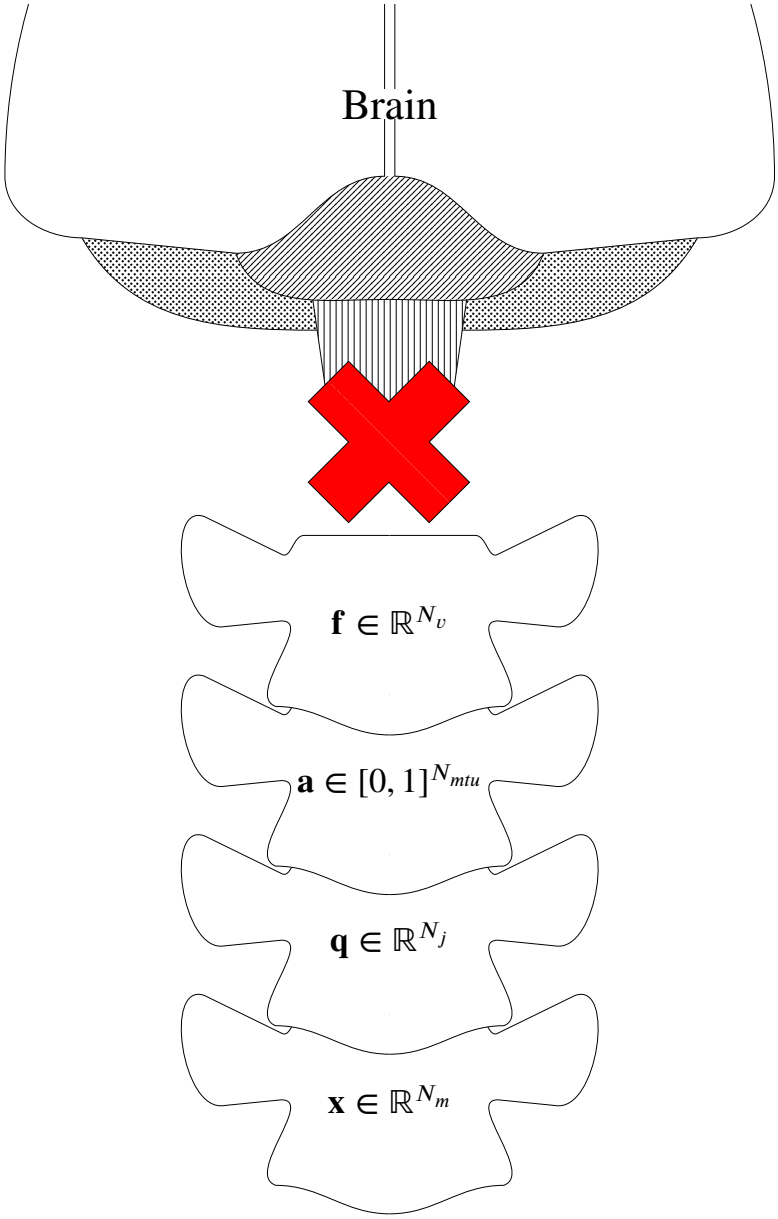

Figure 1.1: The control of the arm can be divided into steps. A healthy subject takes these steps from the top to the bottom in order to control their arm, but subjects with a spinal cord injury -schematized by the red cross here- cannot. In this project, we try to understand the inverse, bottom up, problem: given that we can stimulate the spinal cord, what would be the stimulation frequency required to reproduce the desired kinematics $\mathscr{K}$, of which the observation is $\mathbf{x} \in \mathbb{R}^{N_m}$? The symbols and steps are explained further in the text.

Live animals (*maccaca fascicularis*) were recorded performing reaching tasks with a Vicon motion capture system. The recorded kinematics $\mathscr{K}$ were then gradually processed using a musculoskeletal tool, OpenSim [6], and the Python programming language into the final result: a spatiotemporal estimation of the sensory afferents' firing rates.
Electrical stimulation of the spinal cord is applied locally, following the spatial segregation of muscle motor pools in the spine [7]. An overview of this segregation for some muscles of the NHP's arm is presented in Figure 1.2.

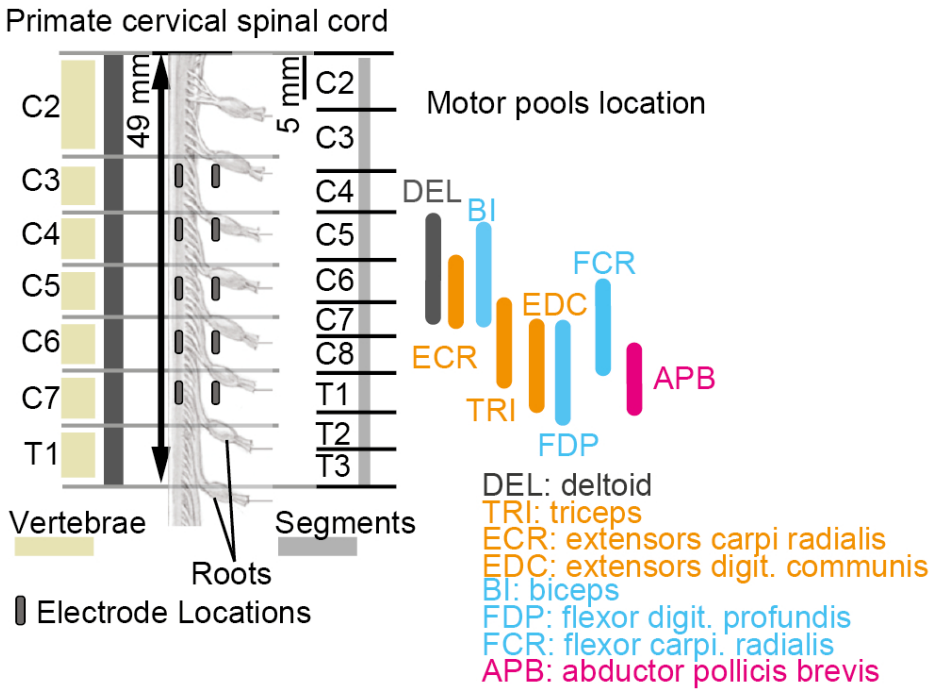

Figure 1.2: Spatial distribution of the motor pools of some muscles in the primate's arm [8].

It is interesting to note that while the direct neural commands are necessary to actuate the muscles, the neural feedback from the muscles to the CNS is critical. For instance, mice of which the sensory afferents had been removed, didn't have a normal locomotion anymore. Furthermore, lesions in the pre motor cortex cause deficits in the ability to direct movements, as the neural feedback is not normally available [9]. Proprioception, or one's ability to be aware of himself (from Latin *proprius:* "one's own" and *capere:* "to grasp"), englobes the fact that we can type on the keyboard or write on paper without looking directly at our hands. In unfamiliar tasks, proprioception is a weaker input for movement control than vision [10]: a child learning to write will constantly look at the paper. With training however, proprioception's importance increases more than vision's, as the brain processes the information faster and learns to take the shortcut.

But the direct benefit of looking at afferent and not efferent fibres in this study is that the epidural electrode will recruit the afferent fibres first before propagating throughout the spinal cord's neuronal circuitry. Therefore, observing the afferent fibres is observing the direct effects of the stimulation. Furthermore, since the natural activity of these fibres is not measurable in real-time, a neuromusculoskeletal model is required to predict them.

1.3 Animal research

A particular aspect of this project is the use of animals, in the objective of developing a therapy for humans. Making a computational model however allows to improve efficiency and refine therapeutic strategies already being experimented on the NHP, eventually lowering the demand for real experiments.
The use of NHP specifically is necessary given the aim of predicting the muscles' sensory afferent firing rates: the strong resemblance they have with humans at both the CNS [11] and musculoskeletal [12] levels permits in-depth motor control comparisons, which are not possible when using other animals such as rats or mice.
The University of Fribourg is one of the two public research facilities in Switzerland to host *macaca fascicularis* specimens, from which we gathered data from two females: Cersei and Sansa. Their treatment in this facility that accumulates over 50 years of experience strictly follows the ethical regulations put in place[1] to protect the animals from misuse in research. Particularly, the macaques population in the facility is limited to 25 so that the open environment in which they live remains uncrowded, and the approved animal research is targeted in order to use the least amount of subjects possible. In further developments of this project the animals will suffer a controlled spinal cord injury which, still following the ethical norms specific to Switzerland, will be reversible [13].

[1] By the Swiss Academy of Biomedical and Natural Sciences.

Chapter 2 Musculoskeletal modelling

In this Chapter we will develop the foundations of the musculoskeletal model, gradually increasing from body parts and joints to muscle modelling as presented in Figure 2.1. Then the mathematical models under which the musculoskeletal model will evolve will be presented, and finally elements to validate the model will be developed.

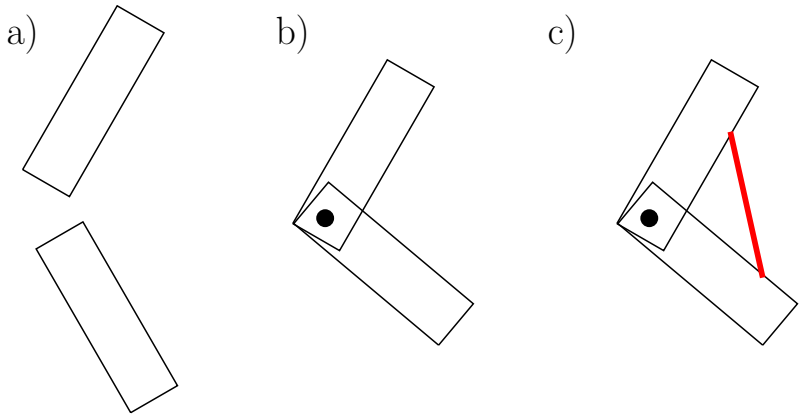

Figure 2.1: Different steps in the making of a musculoskeletal model, and parametrisation at each step. a) Cylindrical segments are defined to represent the bones. b) Joints are added to connect the segments, the simplest joints being rotational. c) Linear actuators representing the muscles are added in order to enable the dynamic evolution of the musculoskeletal model.

2.1 Primate arm model

The first objective of the thesis is to develop a model for a general NHP arm. Briefly, the more physiologically representative the model, the better the predictions [14]. However it is currently unfeasible to build entirely subject-specific models, as some morphological parameters[1] can only be determined in cadaverical studies (at least until more advances in imagery are made). Furthermore, because of the lack of published species-wise morphological data, it is sometimes necessary to refer to data from better studied, closely related species: the *macaca mulatta*, a slightly larger macaque than the *fascicularis* as shown in Table 2.1, and the human. Given the large morphometrical differences between the male and the female macaque, the morphometry of the *macaca mulatta* is considered equivalent to the *fascicularis'* in the construction of a general arm model.

Table 2.1: Average morphometry of the *macaca fascicularis* and *mulatta* [15]:

Animal	Sample size	Weight [kg]	Total arm length [cm]
Macaca mulatta	6 specimens	7.9 ± 3.3	40.1 ± 4.5
Macaca fascicularis	3 specimens	5.7 ± 1.0	31.9 ± 0.6

A previously published, 7 Degrees of Freedom (DoF), male *macaca mulatta* right arm model in SIMM (Software for Interactive Musculoskeletal Modelling), elementarily schematized in Figure 2.2, is used as a basis [5]. As this model was originally developed from an existing human arm, and since human arm models are the focus of a number of previous studies, it seems important to document some differences that were observed between the two species' arms, which is done in Appendix A.

2.1.1 Structural morphometry

The dimensions of the modelled arm are extracted from pictures taken during the dissection of a female *macaca fascicularis* previously done in Fribourg, as shown in Figure 2.3. The extracted segments' lengths[2] and their ratio against the *macaca mulatta*'s are presented in Table 2.2. Without dimensions for the scapula nor the clavicula, the scaling factor of the longest measured segment (the ulna) is used.
The data published for the human arm [16] is used as a reference given the difficulty of estimating the mass of each body segment in a live animal. From the reported segment masses of the human model, the mass distribution by segment is calculated as a proportion of the total mass.

[1] Such as the joints' precise centres of rotation, or the muscle morphometry which is determined by extracting single fibres from the muscle.

[2] These measured lengths are considered standard, while subject specific scaling is eventually done from the Vicon markers and their positions.

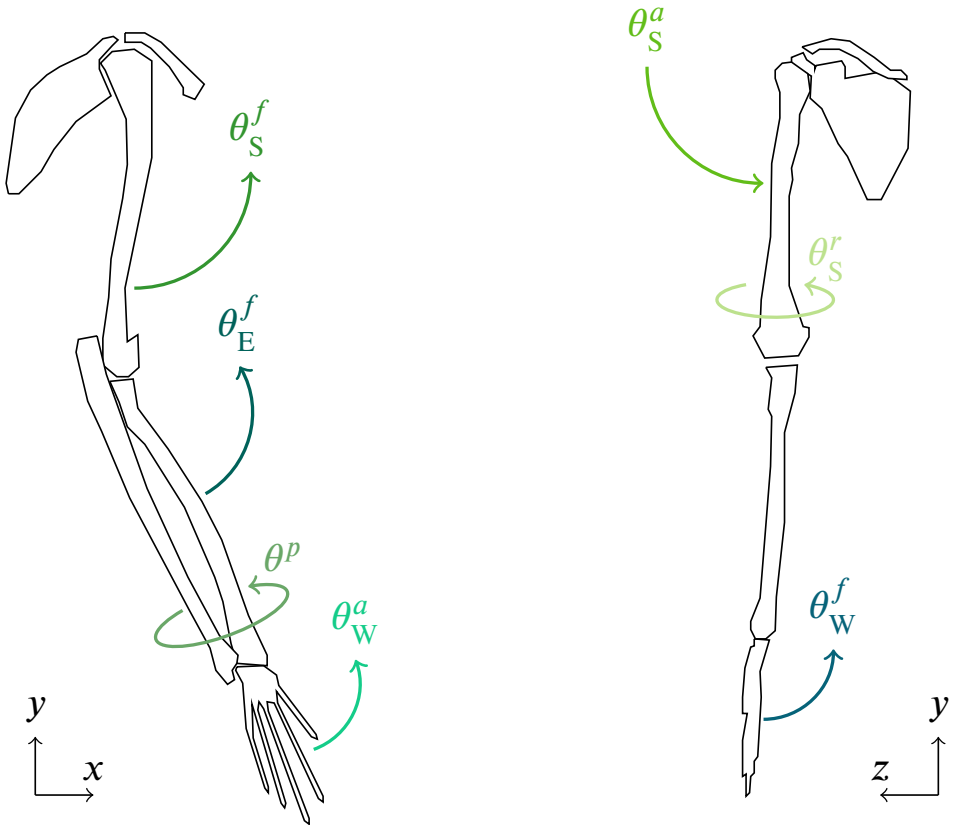

Figure 2.2: Modelled right arm silhouette, lateral and front view. The 7 rotational DoF (the shoulder flexion θ^f_S, the elbow flexion θ^f_E, the radial pronation θ^p, the wrist abduction θ^a_W, the shoulder adduction θ^a_S, the shoulder rotation θ^r_S, and the wrist flexion θ^f_W) are illustrated here with their arrow pointing in the positive angle direction, within the limits defined in Table A.1.

Table 2.2: Body segment lengths, measured in Figure 2.3:

Arm segment	Length [cm]	Scale factor with original model
humerus	10.5 ± 0.1	$.84 \pm 0.01$
ulna (defines the default ratio)	11.9 ± 0.1	$.85 \pm 0.01$
radius	10.8 ± 0.1	$.82 \pm 0.01$
hand	6.4 ± 0.1	$.73 \pm 0.01$

This distribution is then normalized by the largest mass contributor reported in the morphometrical study of the NHP [15]: the upper arm, that makes up to 3.8% of

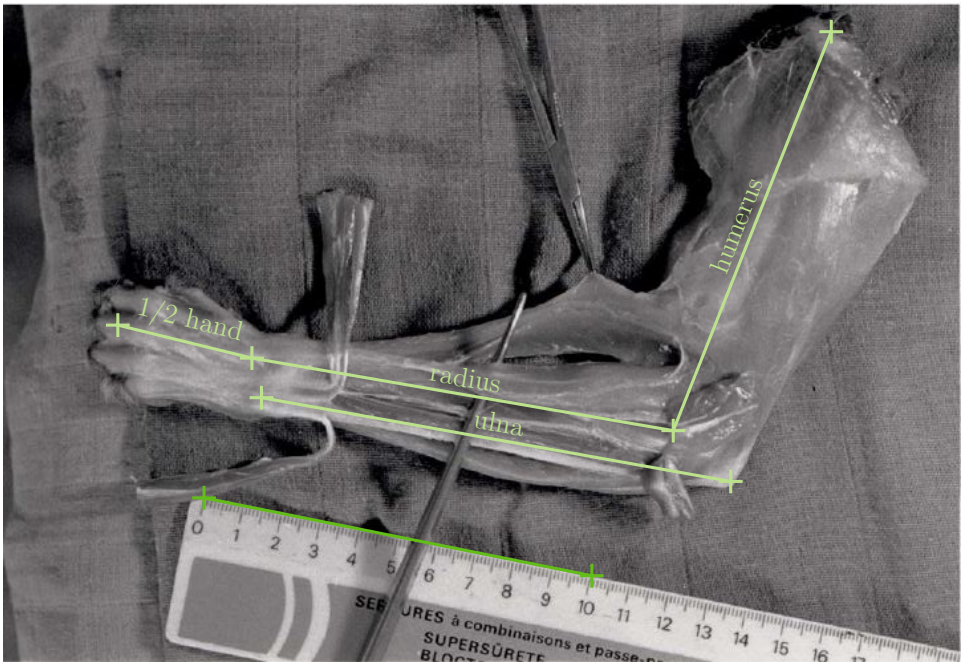

Figure 2.3: A picture from the dissection of a female *macaca fascicularis* gives the modelled arm's dimensions.

the total body weight[3]. The mass distribution is finally scaled to the weight of the *macaca fascicularis* reported in Table 2.1, and is presented in Table 2.3.
This is necessary as the morphometrical study of the *macaca fascicularis* lacks the masses of the scapula and clavicula, and groups the mass of the ulna and the radius segments together in the mass of the forearm. While this is generally reasonable, it is a problem for the model as one DoF, the radial pronation θ^p, moves the radius with respect to the ulna. Either can therefore not be massless.
The inertial parameters are calculated from segment masses and lengths.
Remark: The scapula and clavicula, which are fixed in the model, do not need inertial parameters. These are therefore set to zero until either better data is gathered, or the scapular translation is added (see Chapter 4).
The Centre of Mass (CoM) is reported in the cadaverical study [15] as being at some percentage of the segment length. Considering each segment (humerus, ulna, radius and hand) as an independent cylinder oriented in the segment's longitudinal axis, the CoM is considered to be at the centre of the circular basis at the reported

[3] In the human model, the humerus is 2.00kg while the forearm (radius + ulna) is 1.34kg. Therefore the distribution of the mass between the upper and forearm in the human is exactly the same as the *macaca mulatta*'s, as reported in the cadaverical study. For the *macaca fascicularis*'s arm, the upper arm and the forearm's masses are more similar. As such, the mass distribution of the *macaca mulatta* is used for normalization, until more precise data is available.

Table 2.3: Mass distribution of the model:

Arm segment	Segment mass [% of total body weight]	Segment mass [kg]
clavicle	0.3	0.017 ± 0.003
scapula	1.3	0.074 ± 0.013
humerus	3.8	0.217 ± 0.038
ulna	2.1	0.120 ± 0.021
radius	0.5	0.029 ± 0.005
hand	1.1	0.063 ± 0.011
Total	9.1	0.519 ± 0.091

height. The inertia matrix for these cylinders are then calculated as[4]

$$\mathbf{I}_{xx} = \mathbf{I}_{zz} = m_i \left(\frac{r_i^2}{4} + \frac{l_i^2}{3} \right), \tag{2.1}$$

$$\mathbf{I}_{yy} = m_i \frac{r_i^2}{2}. \tag{2.2}$$

Where m_i, r_i and l_i are the segment's mass, radius and length, respectively.
Remark: The y direction is always the longitudinal axis of the segment, pointing up.
The results are presented in Table 2.4.
Finally, as it is difficult to measure precisely the centre of rotation of the joint angles, those are approximated as being at the insertion point of the next bone. For instance, the shoulder DoFs revolve around the origin point of the humerus.

Joint ligaments

Ligaments are added to the joints as a conditionally activated spring, active when the joint angle overflows the joint limits. A damper mechanism is furthermore added to each joint, from examples found in the human arm model [16]. On the contrary to ligaments, dampers are always active. The damping coefficient, $1.745 \cdot 10^{-4} \frac{\text{Nms}}{\text{deg}}$, is taken one order of magnitude smaller than the humans'.

[4] Where the moments about the x and z axis are taken with those axes passing through the cylinder's basis, and not CoM.

Table 2.4: Inertial parameters for each segment:

Arm segment	CoM [% of length]	CoM [m]	Inertia [kg·m^2]
clavicle	Ø	$0_{3,1}$	$0_{3,3}$
scapula	Ø	$0_{3,1}$	$0_{3,3}$
humerus	51 ± 4	$10^{-2} \cdot \begin{pmatrix} 0 \\ -5.4 \\ 0 \end{pmatrix}$	$10^{-6} \cdot \begin{pmatrix} 903 & 0 & 0 \\ 0 & 213 & 0 \\ 0 & 0 & 903 \end{pmatrix}$
ulna	43 ± 3	$10^{-2} \cdot \begin{pmatrix} 0 \\ -5.1 \\ 0 \end{pmatrix}$	$10^{-6} \cdot \begin{pmatrix} 603 & 0 & 0 \\ 0 & 74 & 0 \\ 0 & 0 & 603 \end{pmatrix}$
radius	43 ± 3	$10^{-2} \cdot \begin{pmatrix} 0 \\ -4.6 \\ 0 \end{pmatrix}$	$10^{-6} \cdot \begin{pmatrix} 114 & 0 & 0 \\ 0 & 15 & 0 \\ 0 & 0 & 114 \end{pmatrix}$
hand	38 ± 2	$10^{-2} \cdot \begin{pmatrix} 0 \\ -2.4 \\ 0 \end{pmatrix}$	$10^{-6} \cdot \begin{pmatrix} 100 & 0 & 0 \\ 0 & 28 & 0 \\ 0 & 0 & 100 \end{pmatrix}$

2.1.2 Musculo-Tendon Units

With the skeletal model defined, its dynamic actuation depends on the attachment of Musculo-Tendon Units (MTU), defined by two extremal attachment points on the bones. Each MTU has a unique line of action, and therefore generates a unique global pattern of segmental angular accelerations [17].
The ability for a MTU to generate a force originates in the model developed by Hill in the late 1950s, described in Figure 2.4.
The MTU is modelled as a Contractile Element in parallel with a passive element (the fibre), mounted in series with a passive element (the tendon). Its characteristic Force-Length and Force-Velocity curves give an idea of how the MTU can generate a force. For instance, the Force-Length curve tells us that the generated force grows exponentially as the muscle stretches.
From this base model several adaptations have been proposed, improving the muscle parametrisation [18] or stability [19]. The latest to date, developed by Millard [20], includes the previous adjustments but also benefits from the resolving of numerical singularities, C^2 continuous response curves[5], and better physiological accuracy (see Figure 2.5).

[5]The C^2 continuity is enforced by using Bézier splines [20].

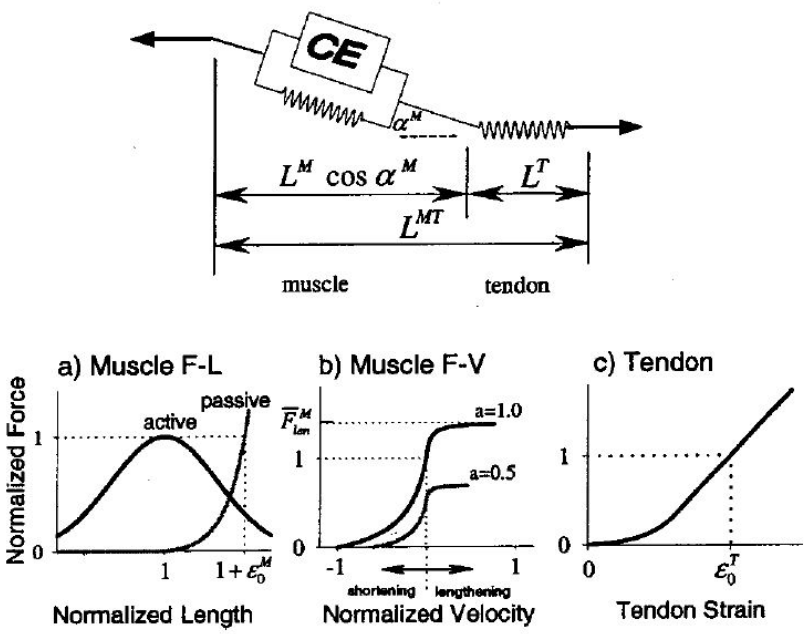

Figure 2.4: Hill-type model, describing musculo-tendon dynamics. Illustration from [18]. CE stands for contractile element.

Each MTU is described by a number of parameters, of which only four are necessary to individually characterize the MTU [22]: the maximum isometric force F^M_{max}, the optimal fibre length l^M_{opt}, the tendon slack length[6] l^T_s, and the pennation angle α_0. The pennation angle should only slightly affect the muscle force solution [23]. On the other hand, the optimal fibre length is expected to be critical. Since the tendon slack length is difficult to measure[7], it is generally adjustable [14] in order to preserve the operating ranges of MTU stretching [16]. While adjusting the tendon slack length, it is important to conserve the ratio tendon length over fibre length [19].
Given an activation $a(t) \in [a_{min}, 1]$[8], and geometric parameters from the skeleton as input, the muscle model predicts the MTU's activation dynamics $\dot{a}(t + \Delta t)$, and outputs the generated force $F^{MT}(t)$, the induced contraction velocity $\dot{l}(t + \Delta t)$, and the fibre length $l^M(t)$, as shown in Figure 2.6.

Activation dynamics:

Given the idealized neural excitation $u(t) \in [0, 1]$, the activation's first derivative is computed as

[6]Length below which the tendon and therefore the whole muscle produces zero force.

[7]It is generally hard to measure even in humans as the limit between the fibre and the tendon is subtle. But given the smaller scale, it is harder to measure in the NHP.

[8]The parameter a_{min} is usually set as close as possible to 0 to avoid singularities.

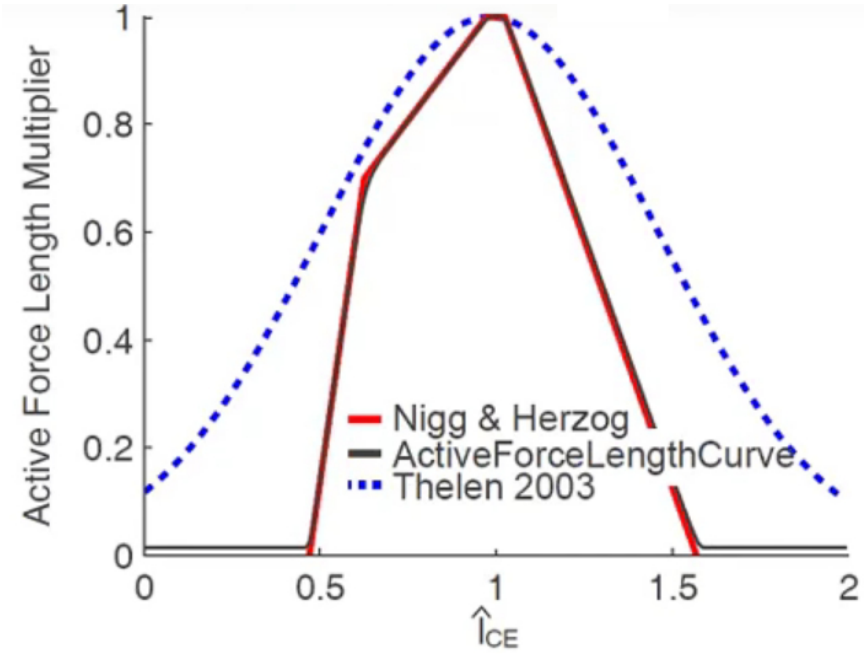

Figure 2.5: Fibre's active force length curve, as reported in the physiological study by Nigg and Herzog, and for the Thelen and Millard muscle models. Illustration from [21]. $\hat{l}_{CE}$ represents the normalized length of the Contractile Element.

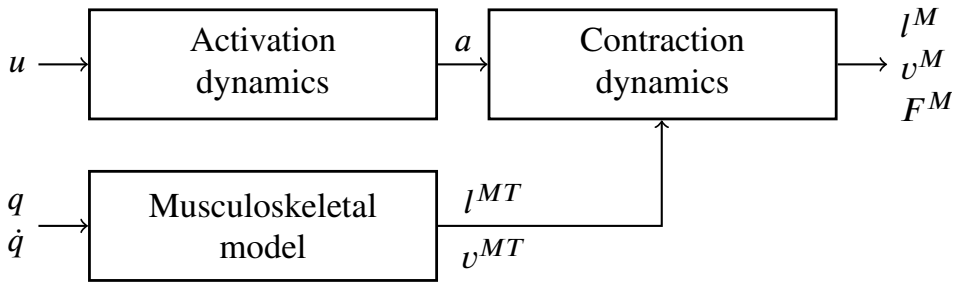

Figure 2.6: The role of the modelled MTU is to predict fibre length l^M, contraction velocity v^M and force F^M from the neural excitations u, and the joint angles q and the velocities $\dot{q}$. An intermediary step is to determine the muscle's activation a, as well as the MTU's length and contraction velocity, respectively l^{MT} and v^{MT}.

$$\dot{a} = \frac{u - \hat{a}}{\tau}, \tag{2.3}$$

where $\hat{a} = \frac{a - a_{min}}{1 - a_{min}}$ is the normalized activation, and τ is a time constant in milliseconds enforcing faster activation than deactivation [18],

$$\tau = \begin{cases} 10 \cdot (0.5 + 1.5\hat{a}), & \text{if } u > \hat{a} \\ \frac{40}{0.5+1.5\hat{a}}, & \text{otherwise.} \end{cases} \tag{2.4}$$

Contraction dynamics:

Using the Force-Length and Force-Velocity curves presented in Figure 2.4, the force is computed as

$$F^{MT}(t) = F^M_{max}\left(a(u,t)\hat{F}^M_l\left(\hat{l}^M\right)\hat{F}^M_v\left(\dot{\hat{l}}^M\right) + \hat{F}^{PE}\left(\hat{l}^M\right)\right), \tag{2.5}$$

with $\hat{F}^M_l$ the Force-Length relation, $\hat{F}^M_v$ the Force-Velocity relation, and $\hat{F}^{PE}$ the passive Force-Length relation (not dependant on the muscle activation a). The hat notation,ˆ, denotes a normalized variable. A force is always normalized with respect to (w.r.t.) the maximum isometric force F^M_{max}, while a length can be normalized w.r.t. either the optimal fibre length l^M_{opt} or the tendon slack length l^T_s.
Under tension, a stretched tendon develops a force according to the Tendon-Force-Length, also presented in Figure 2.4,

$$F^T(t) = F^M_{max}\hat{F}^T_l\left(\hat{l}^T\right), \tag{2.6}$$

where the tendon length l^T is calculated as

$$l^T(t) = l^{MT}(t) - l^M\cos(\alpha). \tag{2.7}$$

Assuming the tendon to be elastic and the mass of the muscle to be negligible (i.e. assuming no inertial forces), the muscle and tendon forces must balance each other:

$$F^{MT}(t)\cdot\cos(\alpha) - F^T(t) = 0. \tag{2.8}$$

This allows to solve the equation (2.5) for $\dot{\hat{l}}^M$ under conditions of inversibility[9]:

$$\dot{\hat{l}}^M = \left(\hat{F}^M_v\right)^{-1}\left(\frac{\frac{\hat{F}^T_l(\hat{l}^T)}{\cos(\alpha)} - \hat{F}^{PE}\left(\hat{l}^M\right)}{a(u,t)\hat{F}^M_l\left(\hat{l}^M\right)}\right). \tag{2.9}$$

Finally, the fibre length $l^M(t+\Delta t)$ is integrated from the contraction velocity.

Remark: Without modifying the formulation of equation (2.9), the contraction velocity is constrained so as to not reach unrealistically short lengths, i.e. below a minimal fibre length l^M_{min},

$$\hat{v}^M = \begin{cases} 0, & \text{if } \hat{l}^M \leq l^M_{min} \\ \dot{\hat{l}}^M, & \text{as computed in equation (2.9) otherwise.} \end{cases} \tag{2.10}$$

Typically, $l^M_{min} = .5l^M_{opt}$.

[9]The lower bounds, $a \geq 0.01$ and $F^M(\hat{l}^M) \geq 0.1$, are set physiologically high, as lower values would make the equation (2.9) stiff.

2.1.3 Muscular morphometry

Parametrisation:

Three of the four parameters (lengths and pennation angle) required to characterize the MTU have been directly measured[10] in *macaca fascicularis* cadavers, for 21 MTUs of the arm [15]. Furthermore, the MTU's Physiological Cross-Sectional Areas (PCSA) were also measured. The maximal isometric force can be calculated from it, by choosing the peak muscle stress at $\sigma = 0.3$ N·mm^{-2} [24], as

$$F^M_{max} = \sigma \cdot \text{PCSA}. \tag{2.11}$$

These parameters are presented in Table 2.5.
However since the arm model contains 39 MTUs, there lacked the parametrization of 18 MTUs. The opportunity came to perform an arm dissection in Fribourg on December 14$^{\text{th}}$. The measurements were more rudimentarily done than during the published morphometrical study, and as such the parameters presented in Table 2.6 should be remembered as generally less trustworthy than those in Table 2.5. That being said, they should be a lot closer to reality than the assumption [5] of default[11] lengths and forces for all missing MTUs. PCSA was estimated by measuring the volume V of the dissected muscle by submerging it under water inside a graduated cylinder: PCSA $= \frac{V}{l^M_{opt}}$. The fibre and tendon lengths were measured without considering the fact that the muscle can be pennate or non pennate. The pennation angle could not be measured. Finally, the measurements were scaled to the dimensions in Table 2.2 as the bone dimensions could be measured. Data was collected for 36 MTUs in the arm. Redundant data with Table 2.5 was generally discarded, except for the pectoralis and latissimus dorsi muscles. These very large muscle are indeed modelled as two and three different MTUs, respectively. This is because the latissimus dorsi, for instance, originates from a large proportion of the spine, and it might be necessary to account for different lines of action inside the whole muscle. Furthermore, this dissection gave valuable hindsight on MTU lines of actions and attachment points, that could then be tuned directly in the model.

Geometry:

MTU insertion and origin points are found in various studies [5], [12], [15], [25]. However beyond those two points, the muscle shape is quite important as well. Primarily, it is important to make sure that the MTU line of action does not cross the skeleton. Especially on the shoulder joint, it is easy to picture a MTU originating from the back of the scapula and crossing several bones as the shoulder internal rotation increases. To prevent this from happening, wrapping surfaces were added to

[10] This morphometric data, relevant for the optimal fibre length, was gathered for a shoulder abducted 90 degrees. As such, it should only be precise when the arm is kept in the horizontal plane [12].

[11] The default parametrisation was: $l^M_{opt} = 20$ cm, $l^T_s = 2$ cm and $F^M_{max} = 29$ N.

Table 2.5: Reported muscle morphometry [15], scaled to our model:

MTU	l^M_{opt} [cm]	l^T_s [cm]	α_0 [deg]	F^M_{max} [N]
bicep long	4.6 ± 0.6	7.9 ± 0.5	11 ± 5	129 ± 48
bicep short	6.5 ± 1.7	5.3 ± 1.4		39 ± 30
brachialis	4.4 ± 1.6	2.1 ± 0.1		66 ± 42
brachioradialis	8.5 ± 3.2	2.8 ± 0.5		54 ± 42
coracobrachialis	1.1 ± 0.2	3.6 ± 2.1	13 ± 12	48 ± 3
deltoid anterior	5.1 ± 0.4	0.1 ± 0.2		45 ± 15
deltoid middle	2.6 ± 0.1	1.9 ± 0.1	22 ± 3	114 ± 27
deltoid posterior	4.4 ± 0.7	1.3 ± 0.3		33 ± 12
dorsoepitrochlearis	5.5 ± 0.7	3.0 ± 0.1		39 ± 15
extensor carpi radialis brevis	2.7	10	12	72
extensor carpi radialis longus	4.7	7.9		123
infraspinatus	2.4 ± 0.3	4.6 ± 1.4	8 ± 11	183 ± 60
latissiumus dorsi	10.6 ± 1.6	7.8 ± 0.6		126 ± 42
pectoralis major	6.8 ± 1.6	0.8 ± 0.4		159 ± 45
subscapularis	1.8 ± 0.3	2.9 ± 0.9	24 ± 11	384 ± 219
supraspinatus	2.9 ± 0.2	3.6 ± 0.5	8 ± 7	111 ± 21
teres major	4.5 ± 0.2	3.3 ± 1.5	16 ± 6	93 ± 30
teres minor	1.3	1.4	10	54
tricep lateral	3.6 ± 0.9	7.0 ± 1.7	27 ± 8	213 ± 81
tricep long	3.9 ± 0.4	6.6 ± 0.4	29 ± 1	243 ± 48
tricep medial	3.9 ± 1.6	2.9 ± 1.0	26 ± 2	99 ± 42

the model. Secondly, the shape of a muscle will obviously directly affect the force vector produced. It was therefore necessary to make several individual customisations, which were documented throughout the year.

Table 2.6: Scaled down muscle morphometry gathered on December 14th (pennation angle is neglected [15]):

MTU	l^M_{opt} [cm]	l^T_s [cm]	F^M_{max} [N]
abductor pollicis longus	11.2	3.8	36.6
anconeus	5.1	0.4	9.2
extensor carpi ulnaris	6.2	7.6	18.8
extensor carpi radis longus	5.5	7.8	51.0
extensor carpi radis brevis	5.1	9.0	23.1
extensor digitorum	7.2	7.8	16.3
extensor digiti	7.8	5.5	9.0
extensor indicis	4.3	4.3	10.9
flexor carpi radialis	3.1	8.6	45.0
flexor carpi ulnaris	11.7	1.6	20.0
flexor digiti profundus	10.1	2.3	41.5
flexor digiti superficialis	9.4	2.7	30.0
flexor pollicis longus	5.9	3.1	40.0
palmaris longus	4.7	7.0	10.0
pronator quad	1.6	0.1	15.0
pronator teres	6.2	0.1	37.5
latissimus dorsi superior	7.8	3.1	51.0
latissimus dorsi central	11.7	3.1	34.0
latissimus dorsi inferior	11.7	3.1	34.0
pectoralis superior	6.2	1.6	188
pectoralis inferior	5.8	0.5	48.0
supinator	6.2	0.9	43.5
subscapularis	6.4	0.8	384
bicep short	10.5	1.5	39
Measurement incertitude	$\pm$ 0.5	$\pm$ 0.5	$\pm$ 9

2.2 Computation chain for the inverse problem

2.2.1 Overview

The inverse problem introduced in Chapter 1 is solved in as many distinct problems as identified steps (Figure 1.1). Figure 2.7 shows the integration of these steps in a unique computation chain. The different tasks are described further in this section except for the last one, which predicts the afferent firing rates and that will be described in Chapter 3.
The subject's kinematics $\mathscr{K}$ are recorded and quantified through the observation of the arm markers positions $\mathbf{x}$. They translate into an initial estimate of the joint angles $\mathbf{q}^0$, from which the muscle activations $\mathbf{a}$ are determined. Now under dynamic constraints, a second estimation of the joint angles $\mathbf{q}^1$ is inherent to finding the muscle activations. From the activations, the firing rates $\mathbf{f}$ are computed.
Each step's solution is not necessarily unique. As such, a first and simple empirical verification of the chain is to feed the muscle activations forward to the model in order to observe the induced joint angles $\tilde{\mathbf{q}}^1$ (expected close to $\mathbf{q}^1$). The problems' dimensionalities at each step are presented in Table 2.7.

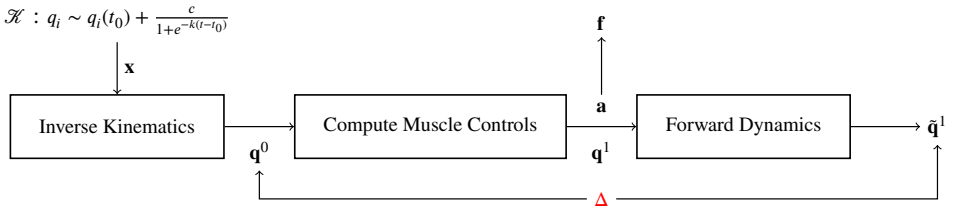

Figure 2.7: Computation chain to solve the inverse problem. The joint angles q_i, $i \in N_j$ are expected to evolve as sigmoids as is experimentally observed [26].

Table 2.7: Problem dimensionality at every step:

Vector	Space	Spatial interpretation	Dimension
$\mathbf{x}$	$\in N^m$	number of experimental markers, 3D	18
$\mathbf{q}$	$\in N^j$	number of modelled DoF	7
$\mathbf{a}$	$\in N^{mtu}$	number of modelled MTU	39
$\mathbf{f}$	$\in N^v$	number of spinal cord segments for arm muscles	7

2.2.2 Motion capture data processing

The experiments are recorded in a controlled environment to ensure reproducibility. Reflective markers are placed on the arm to have their positions recorded via a motion capture system. Likewise, markers are placed on the modelled arm, as shown in Figure 2.8.

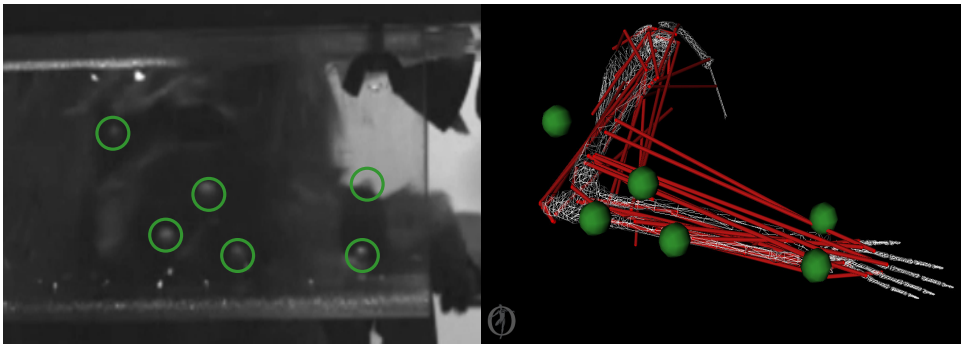

Figure 2.8: Marker positioning on the animal's arm, and on the arm model.

Recorded kinematics are necessarily post-treated individually after each experimental session. The processing done for the kinematics recorded in Fribourg on October, 17$^{\text{th}}$ is presented here.
The data was converted to meters and y and z coordinates are exchanged due to different reference frames. Then, the data's z direction is inverted since the recording was made for the left arm and the model is a right arm:

$$\mathbf{x}_{\text{model}} = 10^{-3} \cdot \begin{pmatrix} 1 & 0 & 0 \\ 0 & 0 & 1 \\ 0 & -1 & 0 \end{pmatrix} \mathbf{x}_{\text{Vicon}} + \left(\mathcal{O}_{\text{model}} - 10^{-3} \mathcal{O}_{\text{Vicon}} \right). \tag{2.12}$$

The offset between the model's origin $\mathcal{O}_{\text{model}}$ (actually the shoulder joint) and the Vicon system's origin $\mathcal{O}_{\text{Vicon}}$ (the centered base of the seat, below the animal) was found empirically at[12]

$$\mathcal{O}_{\text{model}} = 10^{-3} \mathcal{O}_{\text{Vicon}} + \begin{pmatrix} 0.17 \\ 0.25 \\ 0.05 \end{pmatrix}. \tag{2.13}$$

2.2.3 Inverse Kinematics

The least squares method is applied at each time step of the experimental recording to find the modelled marker positions $x_i(\mathbf{q})$ that better match the experimental marker positions x_i^{exp}:

[12]The offset is given in the model's reference frame: with y pointing up and the units being meters.

$$\min_{\mathbf{q}} \sum_{i=1}^{N_m} \omega_i \left\| x_i^{exp} - x_i(\mathbf{q}) \right\|^2, \tag{2.14}$$

where $\mathbf{q} \in \mathbb{R}^{N_j}$ are the model's joint angles which forwardly yield the modelled marker position $x_i(\mathbf{q})$. The weight ω_i of marker i is uniformly set at 1 until relative importance analysis of the markers is made.

Inverse Dynamics

Since the Inverse Kinematics task only considers marker positions, an auxiliary task which considers inertia may be considered for validation. From the joint angles $\mathbf{q}$, velocities $\dot{\mathbf{q}}$ and accelerations $\ddot{\mathbf{q}}$, the joint torques $\boldsymbol{\tau} \in \mathbb{R}^7$ are computed as

$$\boldsymbol{\tau} = \mathbf{M}(\mathbf{q})\ddot{\mathbf{q}} + \mathbf{C}(\mathbf{q}, \dot{\mathbf{q}}) + \mathbf{G}(\mathbf{q}), \tag{2.15}$$

where $\mathbf{M} \in \mathbb{R}^{N_j \times N_j}$ is the system mass matrix, $\mathbf{C} \in \mathbb{R}^{N_j}$ is the vector of Coriolis and centrifugal forces, and $\mathbf{G} \in \mathbb{R}^{N_j}$ is the vector of gravitational forces.
It is important to note that the Inverse Dynamics task is highly dependent on the accurate collection and processing of body segmental kinematics [27], including the derivatives. Namely, the joint velocity is expected to be realistically bell shaped (inherent to a sigmoidal joint angle evolution), as is experimentally observed [10].

2.2.4 Computed Muscle Control

At a new time point t in the simulation time, the objective joint accelerations[13] $\ddot{\mathbf{q}}^*$ are computed using the Proportional Derivative (PD) control law

$$\ddot{\mathbf{q}}^*(t+T) = \ddot{\mathbf{q}}^{exp}(t+T) + \mathbf{k_v}\left(\dot{\mathbf{q}}^{exp}(t) - \dot{\mathbf{q}}(t)\right) + \mathbf{k_p}\left(\mathbf{q}^{exp}(t) - \mathbf{q}(t)\right), \tag{2.16}$$

where T is an adaptive time step and $\mathbf{k_v}, \mathbf{k_p} \in \mathbb{R}^{N_j}$ are the feedback gains[14] on the velocity and position errors, respectively.
The muscle activations $\mathbf{a}$ are used to achieve the desired accelerations $\ddot{\mathbf{q}}^*$, and are computed using the muscle physiology by minimizing the cost function[15] J:

$$J = \sum_{m=1}^{N^{mtu}} a_m^2 + c_0 \sum_{i=1}^{N_j} \omega_i (\ddot{q}_i^* - \ddot{q}_i)^2, \tag{2.17}$$

where c_0 is a constant boolean, that can be set to 1 in order to constrain the joint accelerations when the kinematic input renders the problem stiff, with different weights ω_i for each joint; under the constraint that the torques reproduce the motion:

[13] When achieved, these accelerations drive the model's joint angles towards the experimental joint angles $\mathbf{q}^{exp}$ determined in Inverse Kinematics.

[14] It is recommended to comply to the relation: $\frac{\lambda_i}{2} k_{v,i} = k_{p,i} = \lambda_i^2 = 100, \quad \forall i \in 1, \dots, \mathbb{R}^{N_j}$.

[15] Using an objective function removes the ability to consider individual muscle activation patterns [14]. Furthermore, while minimizing the global energy cost is a widely approved hypothesis as to how the CNS actuates the muscles, this choice has been questioned and wronged at least once [28].

$$\tau_j = \sum_{m=1}^{N^{mtu}} F_m^{MT}(t) \cdot r_{j,m}(\mathbf{q}). \tag{2.18}$$

Where F_m^{MT} is the force produced as in equation (2.5), $r_{j,m}$ is the moment arm of the m^{th} MTU developed about joint j, and τ_j is the torque required around joint angle j as in equation (2.15).
It has been shown that minimizing the muscle stress raised to a power between 1.4 and 5.1 is physiologically analogous to minimizing muscle fatigue [27]. In the present case it was set to 2 as is generally recommended, and because it gave the cleanest results in a static sensitivity analysis.
A Forward Dynamics step is finally done in the window $[t, t+T]$, yielding effective body kinematics. When the torque-induced accelerations are not sufficient to bring the arm close enough to input kinematics it is possible to add reserve torques $\tau_{res} \in \mathbb{R}^{N_j}$ in this Forward Dynamics step, albeit one verifies that the reserves only produce a torque comparatively small to the muscle-induced torques: The reserves cannot be the principal actuators in the motion. As such, the reserves will allow the optimizer to converge, even when the model is not strong enough due to modelling imprecisions.
The whole process described above is then iteratively repeated throughout the experimental time.
The solution found in the CMC is expected to be only as good as the parametrisation of the model upstream, parametrisation which will also highly affect the computation time as the validity of the model determines the possibility of rapidly converging to a solution [16].

2.2.5 Forward Dynamics

The model's equations of motion are integrated forward in time to predict the motion resulting from the application of forces [23]. Knowing the joint torques τ from the last task, the joint accelerations $\ddot{\mathbf{q}}$ are found by inverting the equation (2.15),

$$\ddot{\mathbf{q}} = \big(\mathbf{M}(\mathbf{q})\big)^{-1}\big(\tau + \tau_{res} + \mathbf{C}(\mathbf{q}, \dot{\mathbf{q}}) + \mathbf{G}(\mathbf{q})\big). \tag{2.19}$$

An additional term was however added: $\tau_{res} \in \mathbb{R}^{N_j}$, which is the vector of reserve torques introduced during the Computed Muscle Control.

2.3 Validation

Validation of the model includes checking the C^2 continuity of the fibre, velocity and tendon Force-Lengths; checking that all Force Length curves have no negative stiffness region; and checking that the energy is conserved (fibre work minus fibre strain potential energy matches tendon work minus tendon strain potential energy) [23]. Fortunately, using the recent Millard muscle model already enforced these checkings [20]. Therefore the validation focused on three macroscopic steps: validating the skeletal model, validating the muscle model, and validating the inversibility of computations.

2.3.1 Skeletal model

A study on compensating torques in the human arm is taken as a comparison to our model [26]. In it, human subjects were asked to flex their elbow in the horizontal plane, as is shown on Figure 2.9.

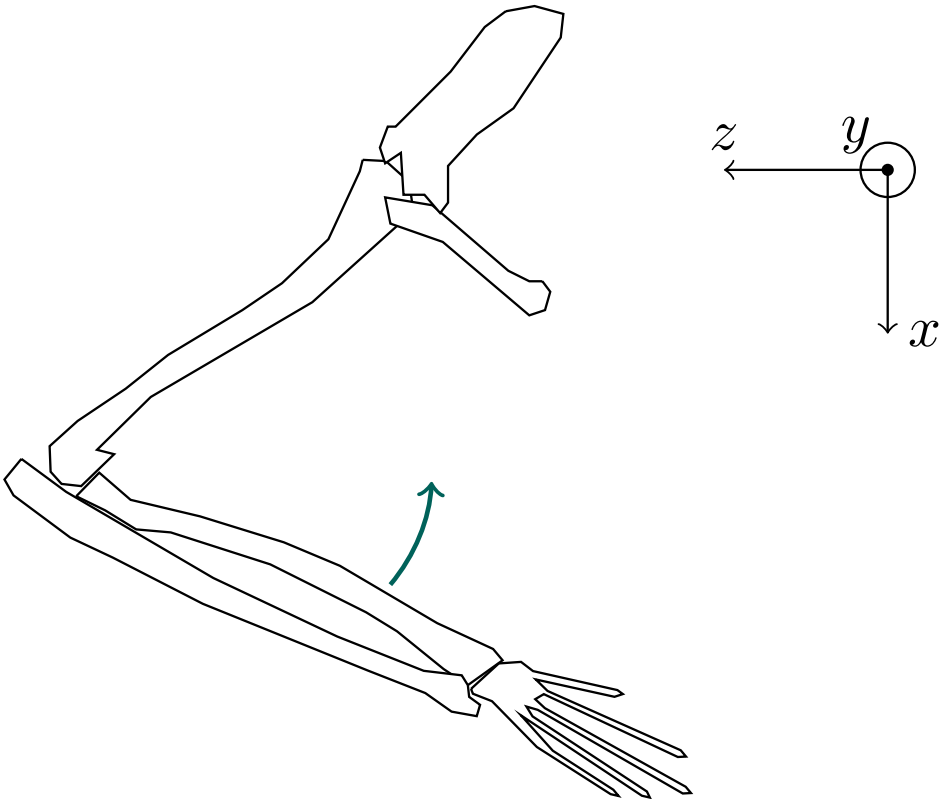

Figure 2.9: Human subjects were asked to flex their elbow in the horizontal plane. Kinematics and EMG were monitored, while torques were manually computed. [26]

Without the experimental recordings, artificial kinematics are created that resemble

them (the details of which is found in Appendix C), and corresponding torques are simultaneously obtained from the simulation and from the formulas:

$$\begin{aligned}\tau_{\theta^f_{\mathrm{S}}} =&\ddot{\theta}^f_{\mathrm{S}}\left(\mathbf{I}^U_{yy}+\mathbf{I}^L_{yy}+m^L l^U l^L\cos(\theta^f_{\mathrm{E}})+\frac{m^L\left(l^L\right)^2+m^U\left(l^U\right)^2}{4}+m^L\left(l^U\right)^2\right)\\&+\ddot{\theta}^f_{\mathrm{E}}\left(\mathbf{I}^L_{yy}+\frac{m^L\left(l^L\right)^2}{4}+\frac{m^L l^U l^L}{2}\cos(\theta^f_{\mathrm{E}})\right)-\frac{m^L l^U l^L}{2}\left(\dot{\theta}^f_{\mathrm{E}}\right)^2\sin(\theta^f_{\mathrm{E}})\\&-m^L l^U l^L\dot{\theta}^f_{\mathrm{S}}\dot{\theta}^f_{\mathrm{E}}\sin(\theta^f_{\mathrm{E}}),\end{aligned}\tag{2.20}$$

$$\tau_{\theta^f_{\mathrm{E}}}=\ddot{\theta}^f_{\mathrm{S}}\left(\mathbf{I}^L_{yy}+\frac{m^L l^U l^L}{2}\cos(\theta^f_{\mathrm{E}})+\frac{m^L\left(l^L\right)^2}{4}\right)+\ddot{\theta}^f_{\mathrm{E}}\left(\mathbf{I}^L_{yy}+\frac{m^L\left(l^L\right)^2}{4}\right).\tag{2.21}$$

Where the dot is the usual notation for the time derivative, and the exponents U and L refer to upper arm and lower arm, respectively.
Figure 2.11 presents the kinematics of this validation experiment. The elbow flexion is increased by about 60 degrees in a sigmoidal manner over a 0.2 seconds period, ensuring a bell shaped velocity profile.
Figure 2.10 presents the comparison between manually computed torques and results from the simulation. The simulated elbow torque includes effects from the joint's damping which is resistive to the movement. Hence the positive shift observed on the elbow torque: more is required to actuate the elbow than what had been computed with idealized mechanics.

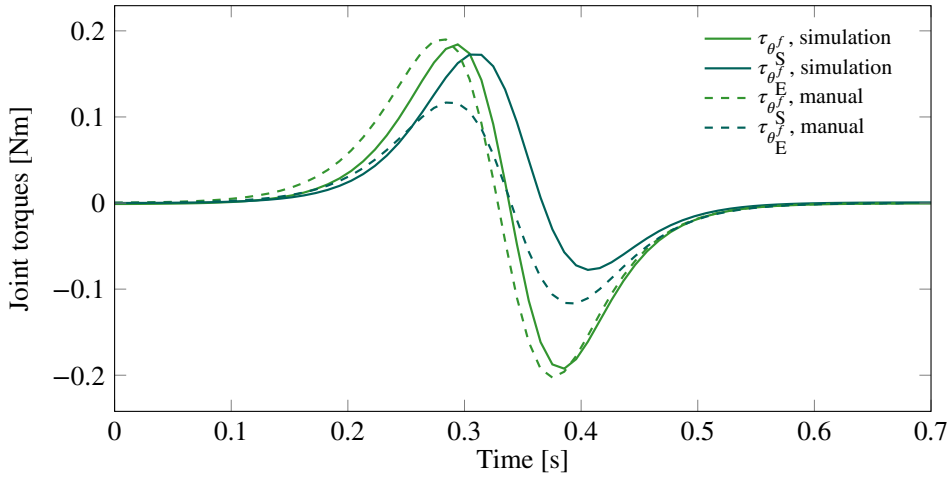

Figure 2.10: Verification of torques during Gribble's 1DoF experiment involving a horizontal elbow flexion [26]. The difference in elbow torque is explained by the addition to the model of a damper inside the elbow joint.

Quantitatively, the damping coefficient for the elbow flexion was set at $1.745 \cdot 10^{-4}\,\frac{\mathrm{Nm}}{\mathrm{deg}\cdot\mathrm{s}^{-1}}$, i.e. one order of magnitude smaller than what had been set in a similar

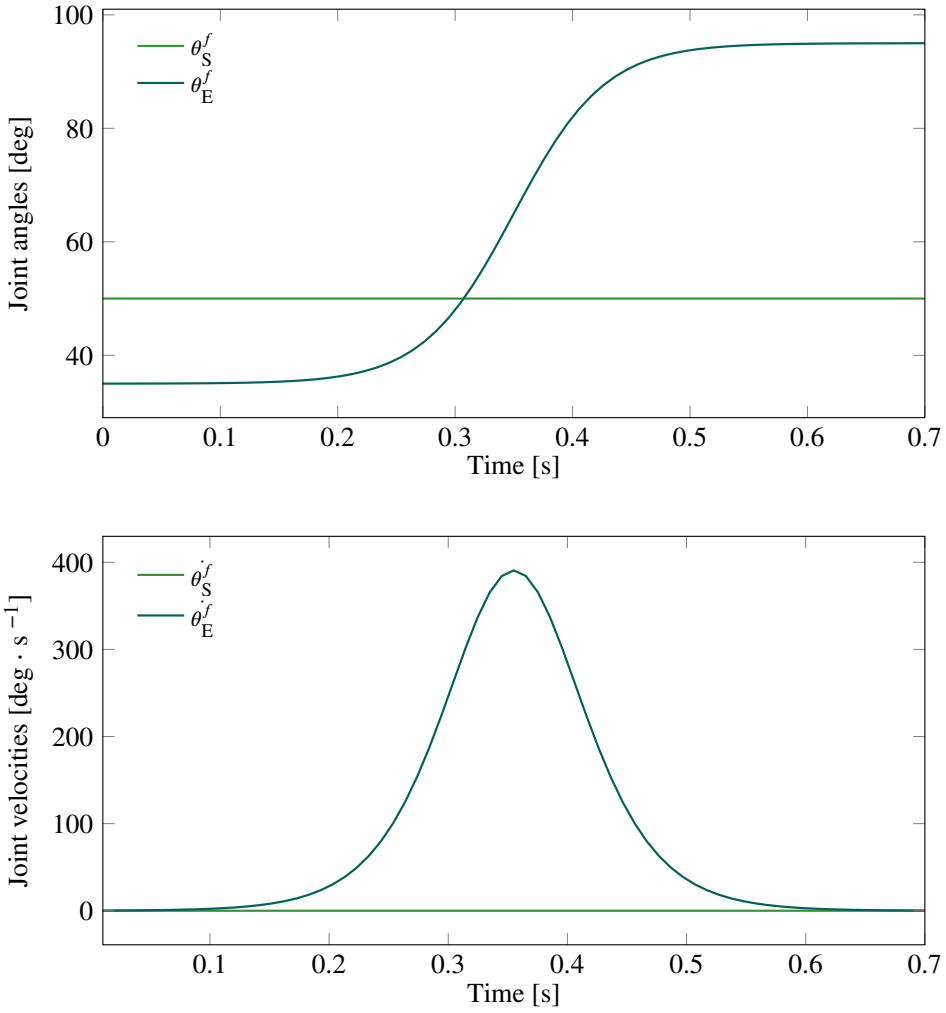

Figure 2.11: Joint angles and velocities for the first validation experiment, reproduced from [26], albeit the signs are inverted due to different conventions in defining the neutral positions.

human arm model [16]. Multiplying it by the peak joint velocity 400 deg·s^{-1} read in Figure 2.11, we obtain about $7 \cdot 10^{-2}$ Nm, which is in coherence with the peak shift observed in Figure 2.10.

2.3.2 Muscular model

EMG Data

Simultaneous recordings of arm kinematics and muscle activity (EMG), courtesy of Prof. Lee E. Miller and Raeed Chowdhury, are used to validate the muscle model. The recordings correspond to centre-out tasks performed by primates in 3 dimensions with four possible target directions at the cardinal points. Kinematics were recorded at 100 Hz, while EMGs were recorded for 22 MTUs[16] of the upper limb at 2 kHz with an anti-aliasing filter at 500 Hz. EMGs were then high-pass filtered at 10 Hz, rectified, and low-pass filtered at 20 Hz.
Recordings of 279 successful tasks were shared, each of them lasting less than 1 s. Subjects reacted to an oral command to start the task, which is taken as the time 0. 69 out of those 279 recordings required the animal to centre-out the handle away from himself in the frontal direction. This specific subset is taken as the validation experiment, during which the arm evolution is schematized in Figure 2.12.

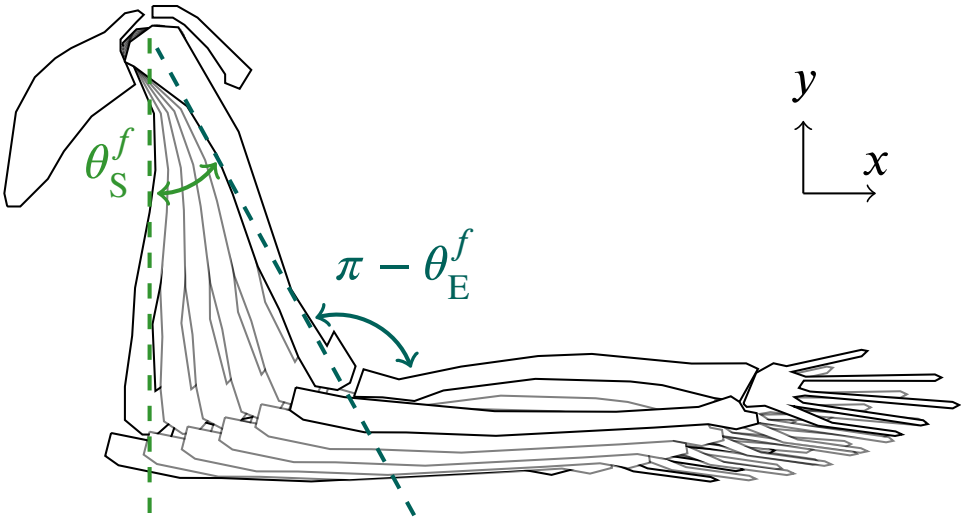

Figure 2.12: Arm evolution in the frontal-directed centre-out task. Essentially two joints are moving: the shoulder and the elbow flexion.

Corresponding kinematics are quantitatively shown in Figure 2.13. The free-from character of the experiment appears obvious. Furthermore, one notices a clear distinction between the two phases the task can be divided into: the "preparation" and the "reaching" phases, as Miller named them [4].

[16]Only one of them, the trapezoidal muscle, is not presently modelled and therefore dropped.

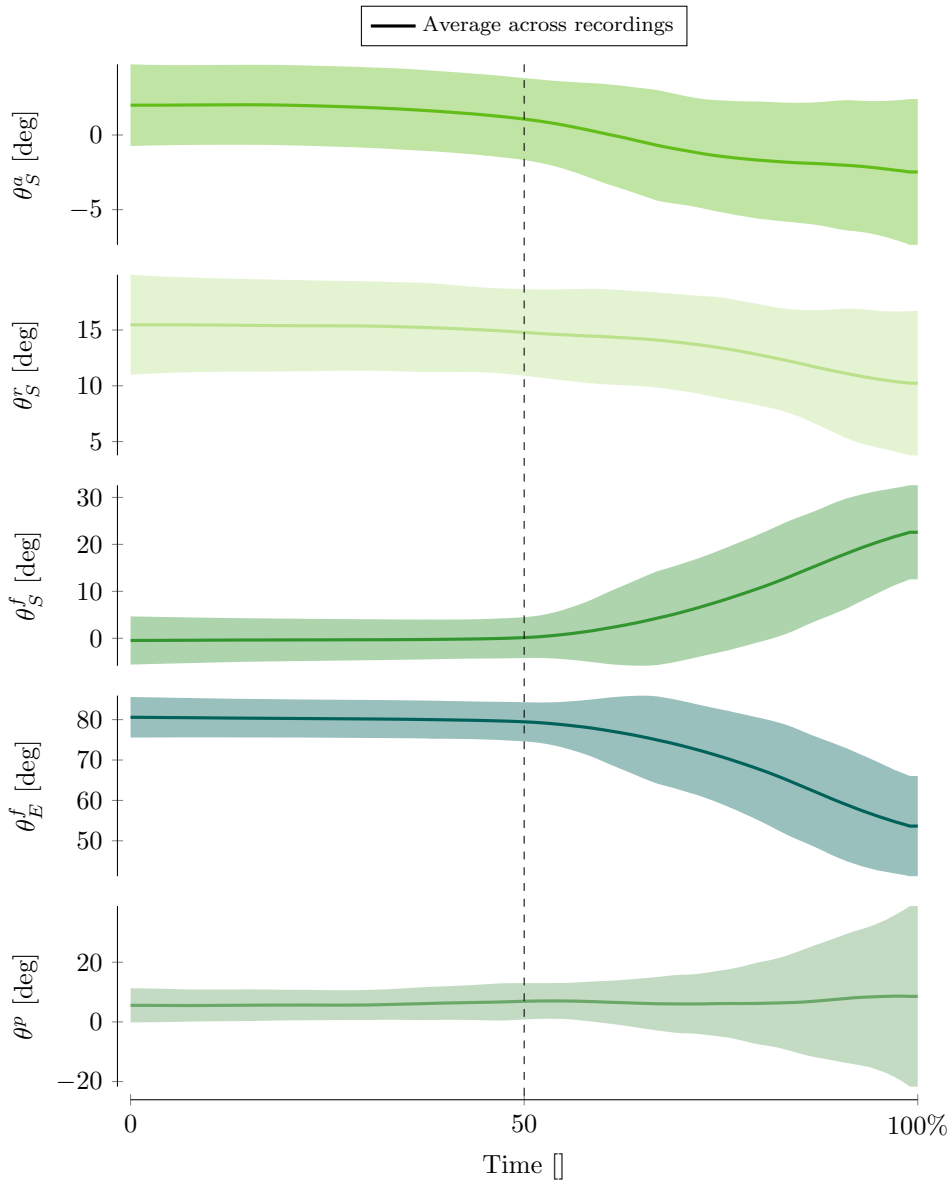

Figure 2.13: Joint angles during the centre-out task in the forward direction (positive x). The centre out task may be divided in two major phases: a static phase in the first half, followed by a "reaching" phase after that can be characterized by a simultaneous elbow flexion and shoulder extension. The free-from character of the experiment is put in evidence by the shaded areas, that represent $\pm$ 2 Standard Deviations around the average. The dashed vertical line represents the phase separation between preparation and reaching.

Variability between EMG recordings

The EMG recordings are normalized since their amplitude is too dependent on experimental conditions, such as electrode placement on the muscle.

Furthermore, and despite the processing done, EMG signals are extremely irregular. One therefore wonders what is the variability observed between EMG recordings of the same task, with the same target direction. In other words, it is interesting to find out up to which precision it is meaningful to compare for a MTU the computed muscle activity with the recorded EMGs.
The correlation and variance of each recording with every other one are iteratively computed. The averages are then taken across 4761 correlations[17] and variances, respectively. Figure 2.14 presents them, allowing to identify muscles which should be considered for the validation of the model and computations.
We also present statistical trends, computed across all recordings, for the EMGs of three muscles identified as highly coherent[18], middly coherent or incoherent, in Figure 2.15. One notices that the long head of the biceps is on average, constantly un-recruited during this task, therefore explaining why it is so little self-correlated: the signal is mostly noise.

Custom signal processing

Kinematics are fed to the model and the simulation predicts muscle activations at time steps that are unpredictable, since their spacing answers to the optimizer's needs. Hence the muscle activations are eventually resampled on the recorded kinematics time points, as they are the cardinality bottleneck. But before, the activations are filtered using a Savitzky-Golay filter (window length .1s, i.e. 11 points at 100 Hz, polynomial order 2), as the main weakness of the generated signal is the presence of peaks due to the numerical computation. The activations are then normalized: as it is difficult to measure individual muscle activity via a surface electrode's EMG [19], muscles were surgically implanted with electrodes. However, the EMG amplitude cannot be taken into account for comparison: depending on the electrode placement, the signal's strength is variable. Therefore the EMG recordings are normalized, and so must be the activations.

Comparison

The two signals of EMG and muscle activation are by essence too sensitive to be reliably and generally compared. Previous works therefore focused on using peak correlations and time of the peaks as comparison metrics, after accounting for the delay between EMG and activation [4] [23], or qualitatively validating the resemblance [29]. The electromechanical delay of a muscle, defined as the interval be-

[17] There are 69 recordings, hence there are $69^2 = 4761$ inter-correlations.

[18] In the sense that their EMG across the recordings is highly correlated. This implies that they are important to the motion, and coherently recruited throughout the trials.

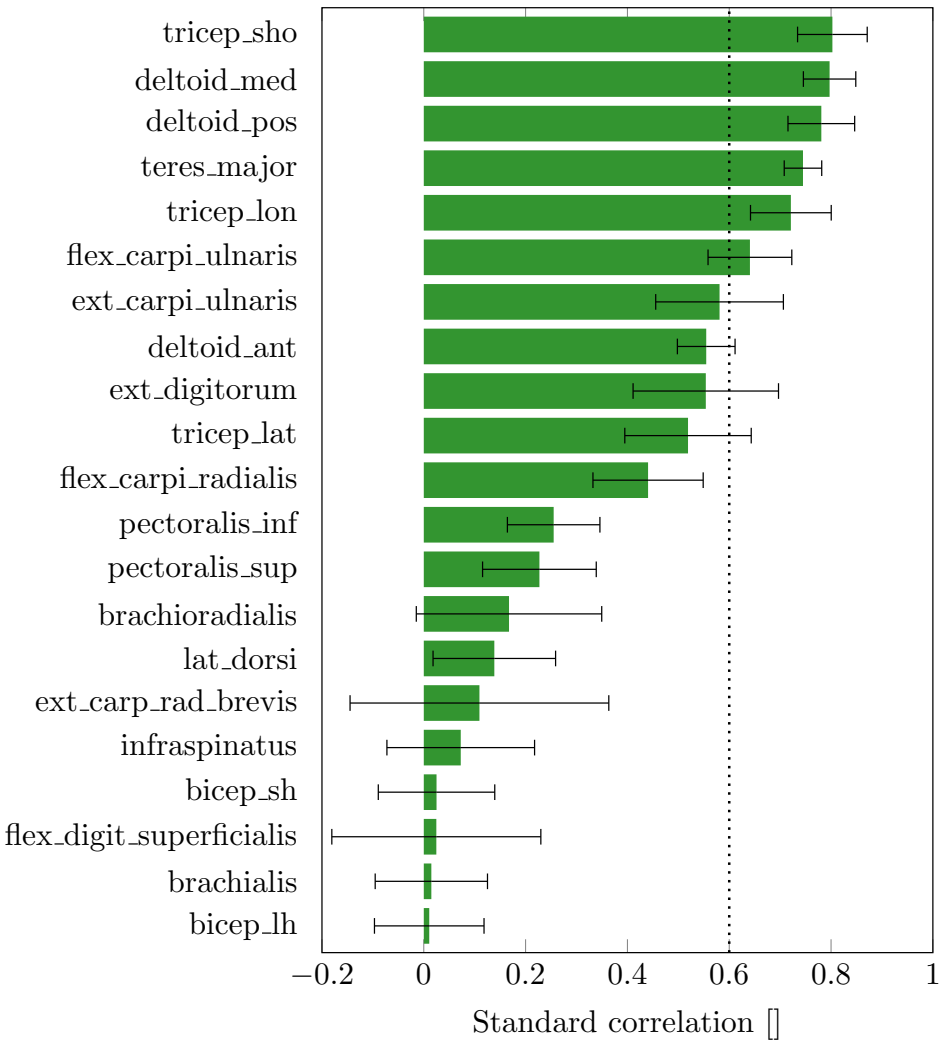

Figure 2.14: Average standard correlation across recordings of each muscle's EMG, frontal centre-out task. The error bars represent ± the average variance. The dotted vertical line highlights an arbitrary confidence threshold. The EMG recordings are presented for a few muscles in Figure 2.15.

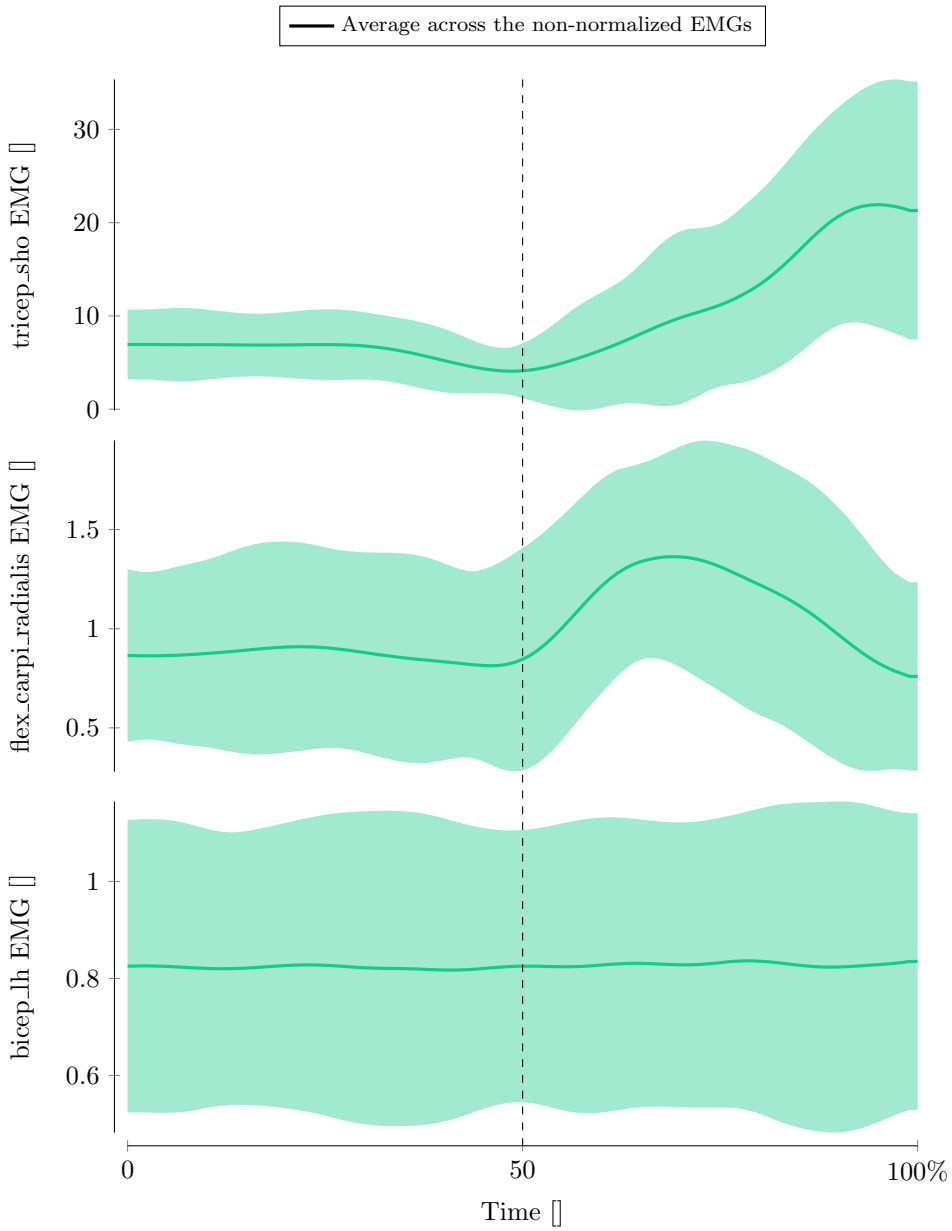

Figure 2.15: Frontal centre-out task: statistical trends of EMG signals, computed across all recordings for three muscles whose normalized EMGs were highly correlated, middly correlated, and uncorrelated, respectively. The shaded areas around the average represent ± 2 Standard Deviations. The dashed, vertical line represents the phase transition between preparation and reaching.

tween the onset of the myoeletric activity and the onset of the resulting change in the mechanical variable observed (movement or force for instance) ranges in humans from 25 to 100 ms, depending on the muscle and the task [30].
Peak cross-correlations are computed as the maximal value

$$\max_{\Delta t} \int_{t_0}^{t_f} \mathrm{EMG}(t) \cdot a(t + \Delta t) dt, \tag{2.22}$$

where Δt is a time shift smaller than 0.10 second, t_0 and t_f are the start and final time of recording, and EMG and a are the muscle's EMG and predicted activity, respectively. The cross-correlation is by definition non-commutative, and the predicted muscle activity a is allowed to be delayed to match with the measured muscle response, i.e. the EMG.
Figure 2.16 shows peak cross-correlations computed in a singled out frontal centre-out task (ID 2). The EMGs and activities seem highly correlated except for the teres major.

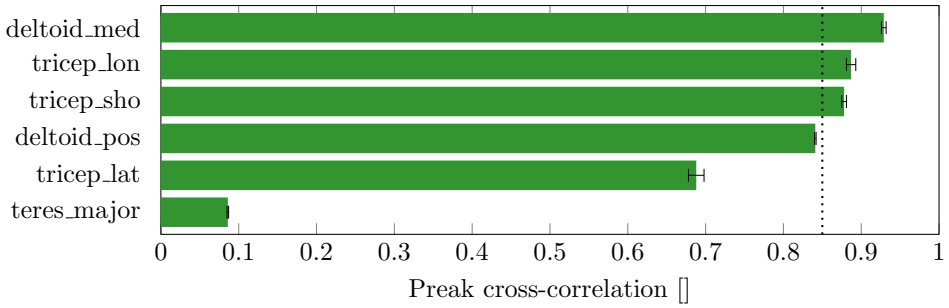

Figure 2.16: Peak cross-correlations computed for MTU selected on their EMG consistency, frontal centre-out task, recording ID 2. The dotted vertical line highlights an arbitrary confidence at 0.85.

The two processed signals, EMG and predicted muscle activity, are shown in Figure 2.17. A starting time window of 0.05 s is cut from the result, as it is used to initialize the simulation. One notices that the correspondence is better in the reaching phase than in the preparation phase, principally because of the teres major. Indeed it seems that the latter's initial activation coincides with strong activation of the pectoralis superior in the preparation phase. Co-contraction of antagonist muscles in still posture is difficult to model, and this is amplified by us not taking into account in the model that the animal was holding a handle throughout the centre-out task. Already grasping the handle could be the cause of these muscles recruitment, but it is not reproducible with the posture-based recruitment principle used in simulation. On other muscles, we notice that the recruitment order follows that of the live animal: the lateral head of the triceps is recruited first, then the short head, and finally the long head. However the lateral head's pattern of recruitment differs slightly as we predicted a peak of small amplitude followed by a peak of large amplitude[19],

[19]This could point towards an overestimation of the MTU's maximal isometric force.

while during the experiment the lateral head is continuously recruited. This could explain the lower cross-correlation value computed for this head of the triceps. Eventhough the lower cross-correlation obtained for the tricep lateral head is less of a concern, as the latter was already the least consistently recruited muscle of the selected few in the experiments (Figure 2.14).

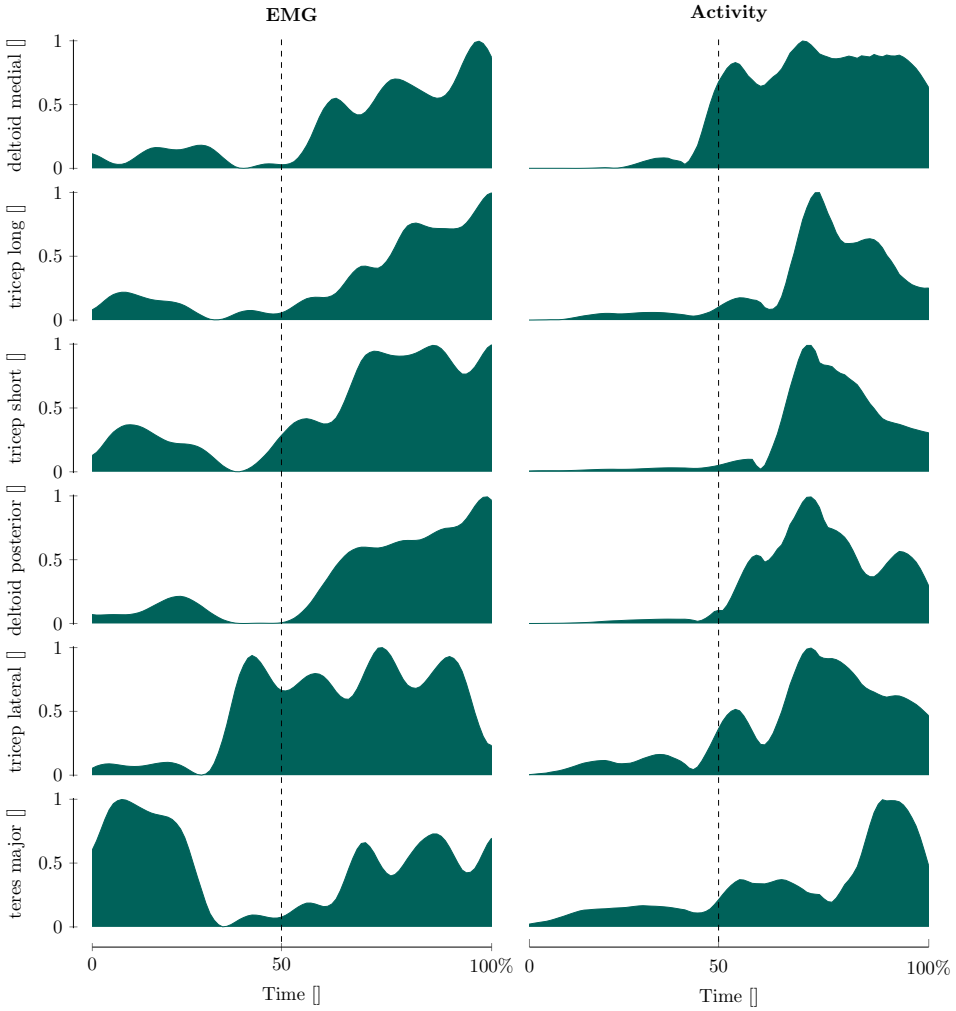

Figure 2.17: Processed EMG recordings and predicted muscle activities during the frontal centre-out task ID 2, for MTUs selected on their EMG consistency in this specific task. The dashed line represents the phase change between preparation and reaching, observed in kinematics: Figure 2.13.

In order to better comprehend the situation, the joint angles, computed muscle activities, and their moment arms are presented in Figure 2.18. It appears that, without antagonist co-contraction, the lone teres major's activation during the preparation phase would displace the arm, since the latter's shoulder flexion moment arm is

significant.
As such it confirms that it is not necessary to activate it in the simulation during the preparation phase. As there is no motion, one verified guess is that the teres major's activation is resulting from a co-contraction with the pectoralis superior, whose action on shoulder flexion is opposite to that of the teres major. Furthermore during the motion itself it was shown in an other study that there is no significant evidence of antagonist muscles co-contraction, at least around the shoulder joint [31]. It therefore appears that the simulation reproduces rather closely the experimental data.

2.3.3 Forward simulation

Finally it is possible to feed the model with the computed muscle controls and compare the resulting kinematics with the original ones. It is first presented for the frontal centre-out tasks, and then for the indigenous recordings of a three-dimensional reaching and grasping task.

Centre-out task

Figure 2.19 presents the joint angles at different steps of the simulation, while Figure 2.20 presents the outcome of the forward computation and compares it with the ensemble of frontal centre-out task recordings at our disposal. Numerical errors do propagate as simulation time increases, during the computation of muscle controls. As such, it is not surprising that the solution deviates more at the end than at the beginning. However, the model appears strong enough to reproduce original kinematics, even when closing the loop with the forward computation. It is appreciable that the solutions at all the computational steps are within two standard deviations of the experimental data computed between the recordings at our disposal.

Reaching and grasping task

A second task is recorded in Fribourg. Unlike the centre-out task, the reaching and grasping is three dimensional and since it is custom-made, videos of the recordings are available, allowing to visually validate the reproduced kinematics too. It also has the benefit of being longer (the typical reaching, grasping and returning lasting about 4 s), allowing the simulation to better stabilize. The motion-captured kinematics (marker positions) are used as is, without signal processing other than the transformation explicited in equation (2.12). However, a 6Hz low-pass filter is applied to the computed joint angles before starting the computation of muscle activities, primarily to smoothen the underlying joint velocities.
Reproduction of the input kinematics at the different steps of the simulation are presented in Figure 2.21. One can see that the model is able to reproduce the three-dimensional kinematics just as well as the two-dimensional ones. The higher correspondence between CMC and FD outputs is explained by time constraints: sampling frequency out of CMC is about 2kHz, and it was possible to include in the

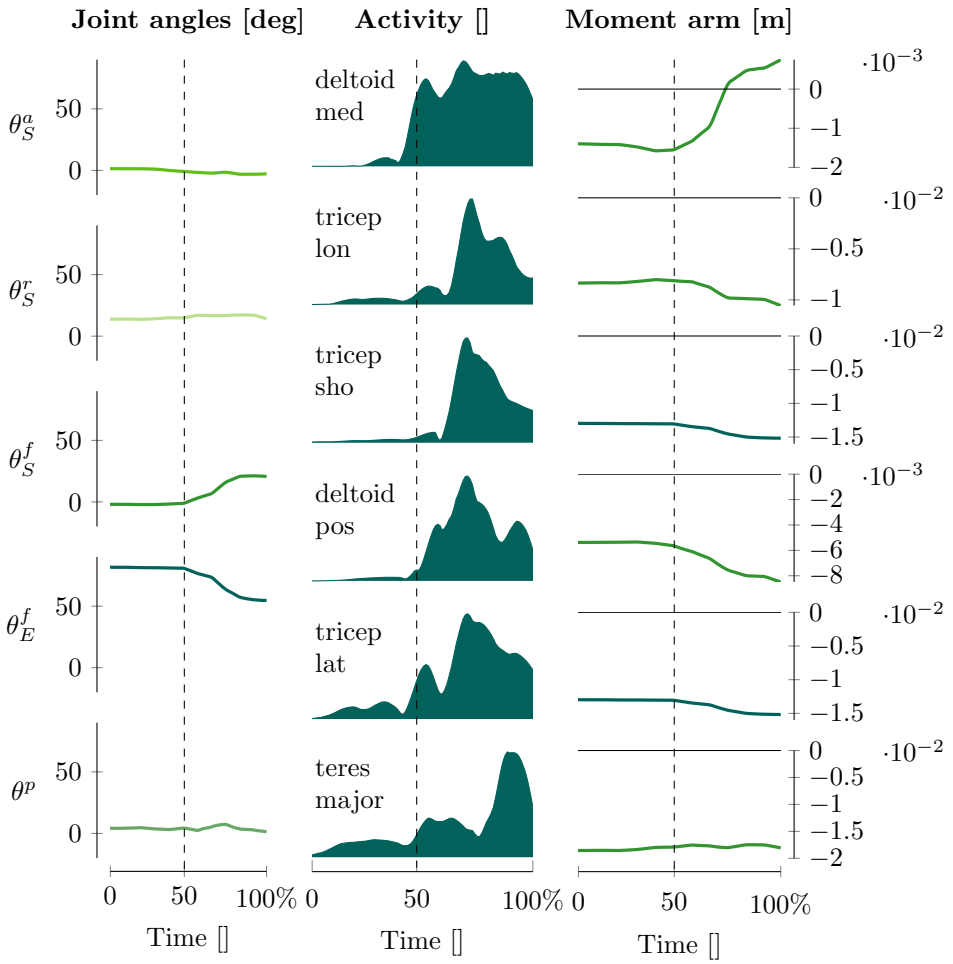

Figure 2.18: Joint angles, computed muscle activities, and moment arms for the most relevant DoF (either shoulder flexion or elbow flexion, indicated by colour). The dashed, vertical lines represent a phase separation between preparation and reaching. The teres major is a significant contributor of shoulder flexion moment.

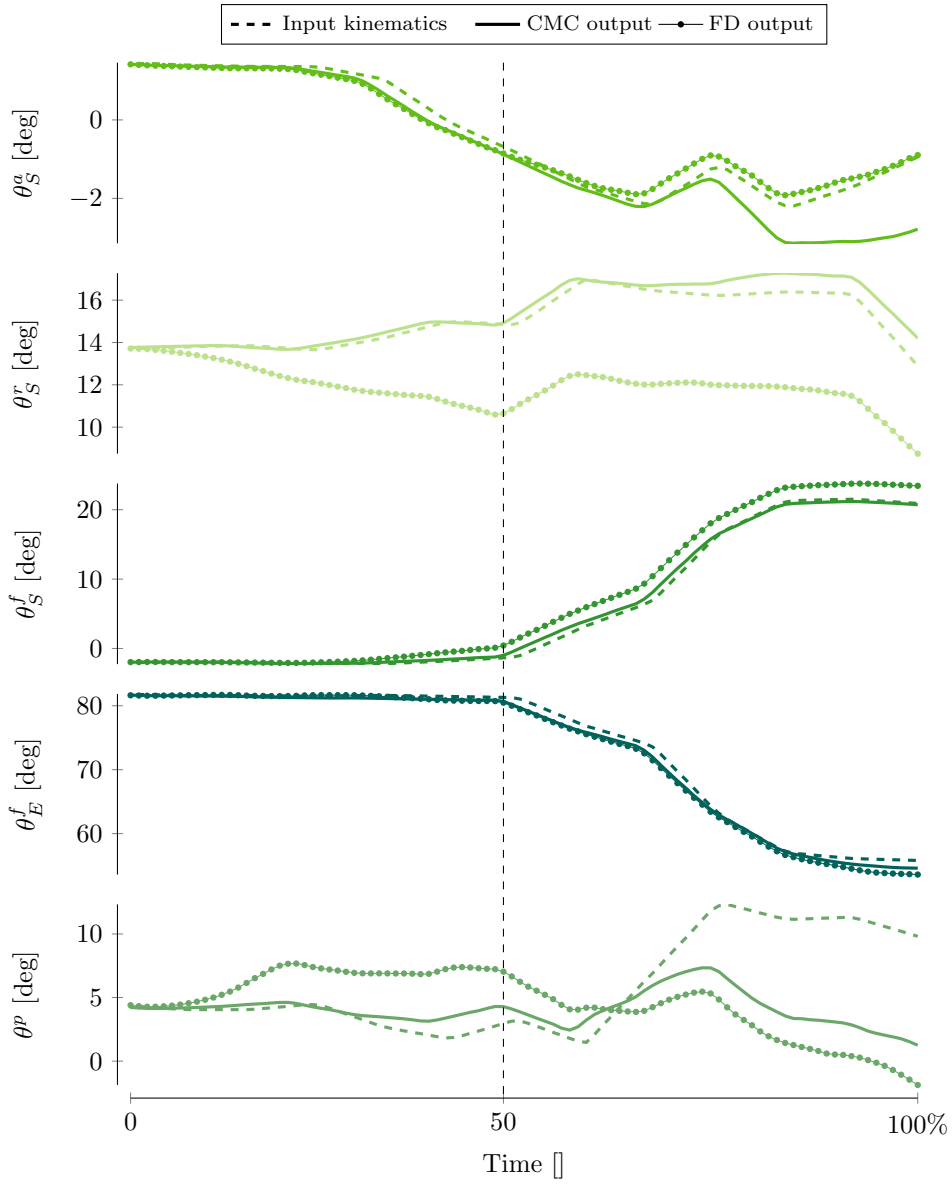

Figure 2.19: Principal joint angles at the three steps of the computation loop, two-dimensional experiment.

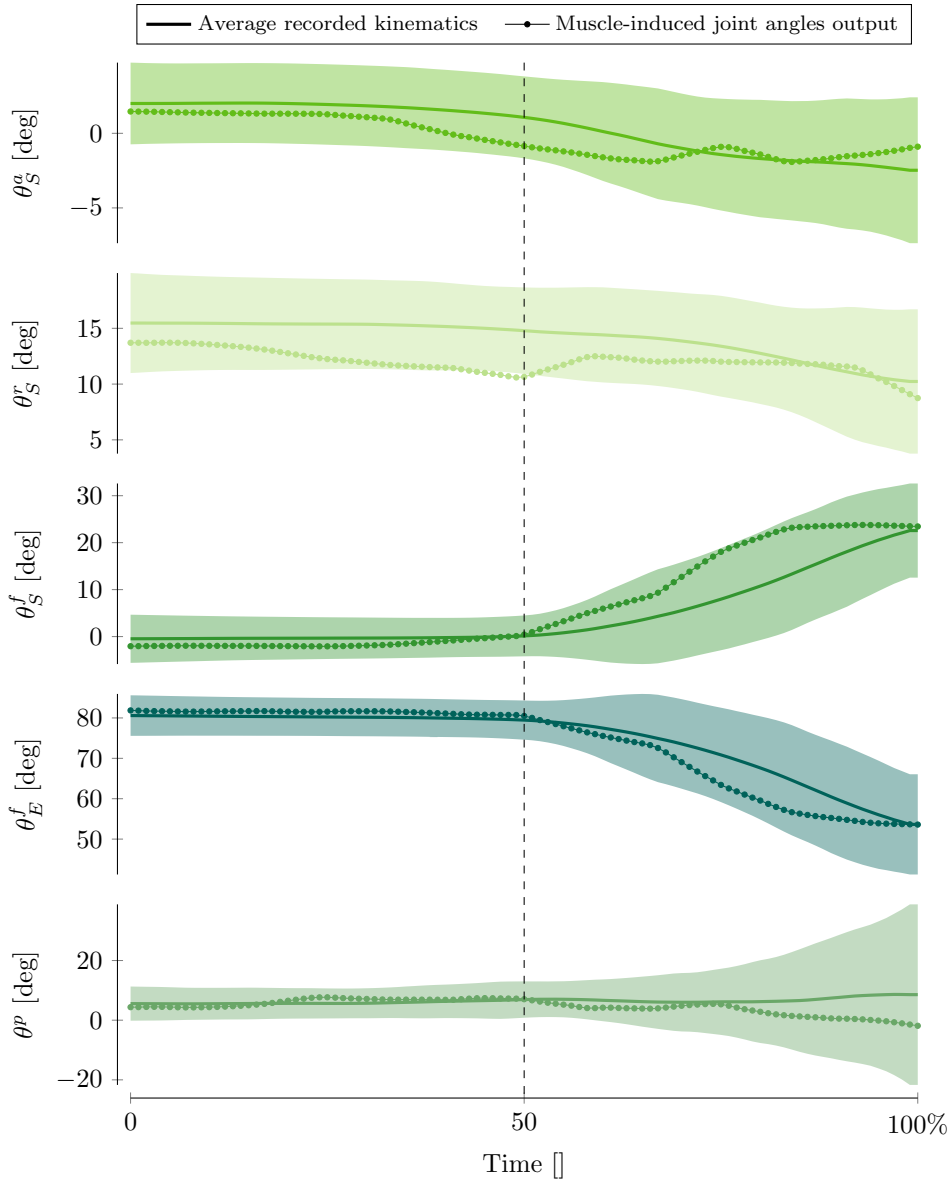

Figure 2.20: Principle joint angles retrieved after the forward dynamics step, and comparison with the average frontal centre-out trajectory. The shaded area corresponds to ± two standard deviations between recordings.

computation 0.5 s buffers before and after the singled-out reaching and grasping task presented. These buffers allow the forward simulation to stabilize very well.

2.4 Limitations

The model does not allow scapular translation, which can eventually be problematic, for some motions spanning a larger area than during available recordings.
The joints are ideally modelled as perfectly decoupled rotations. That is not physiologically correct, and this poses the issue of the model being theoretically usable in unrealistic motions: the shoulder adduction range for instance, is not dependent on the shoulder flexion. But the real arm's freedom would not be the same when the arm lies parallel to the body or perpendicular to it.
In general, any model idealizes the reality to the simplest possible approximation. However, in such a problem as ours it becomes difficult to estimate where to situate the simplest possible approximation, and that for each aspect of the modelling. As such it is necessary when looking at the validation to keep in mind the number of assumptions made, and the parametrization dimensionality. Extensive work is being done to get the most physiologically accurate parameters, as is the focus of morphometrical studies, but also of more advanced developments: results obtained in the optimization of a human arm model have been recently presented [32]. But such a study was only possible because of the amount of morphometrical data available for humans.
Results shown also included OpenSim's reserve actuators, which are extra torques that can be used when the muscle model is not able to produce the motion by its own produced torque. Their use should however be at least one order of magnitude lower than the desired torque. While removing them did not terminate the model's ability to reproduce the motion, it was chosen to keep them activated on shoulder joints, to compensate for the lack of scapular translation in wider motions.
Finally, the free form nature of the recorded experiments remove the possibility of considering a typical task and to validate the model's muscle activations on more than one recording at a time.

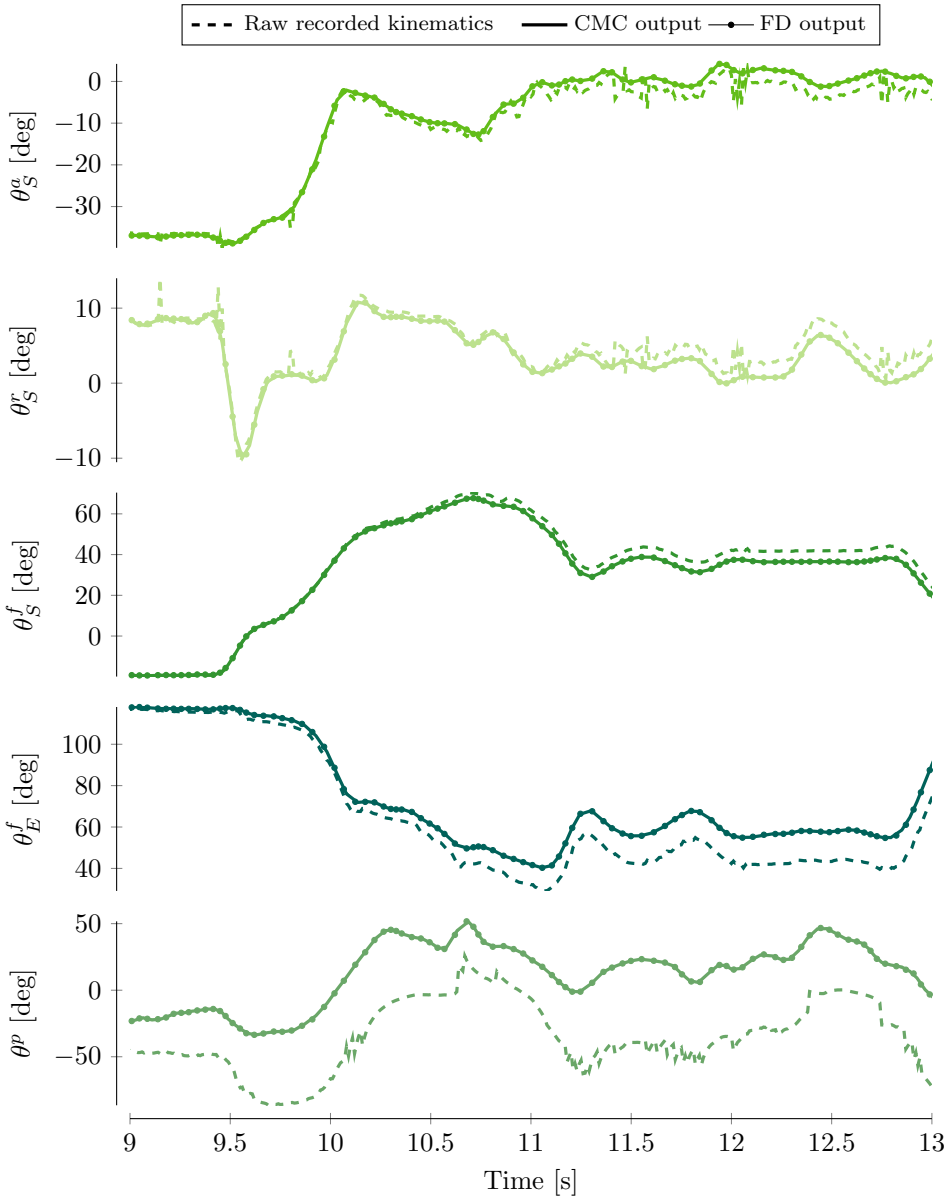

Figure 2.21: Principal joint angles at the three steps of the computation loop, three dimensional experiment.

Chapter 3 Spinal cord stimulation strategy

3.1 Theoretical introduction

In this section the physiological muscle control by the CNS and the Epidural Electrical Stimulation are introduced. The link to the present thesis is made, then NHP spinal data is presented and modelling considerations are stated.

Natural motor control and Spinal Cord Injury

Motor control over the limbs normally flows through the spinal cord down from the brain. The communication between the brain and the actuators is of course interrupted in case of a Spinal Cord Injury (SCI). However the damage remains localized, and it has been shown that below the injury remains the necessary and sufficient neuronal networks to coordinate locomotion [33]. Furthermore it appears that in many SCIes there remains enough intact neural tissue to allow for recovery.

Epidural Electrical Stimulation of the lower neural network

The approach initiated by Prof. Courtine to restore limb control emphasizes stimulating the dormant[1] neural network below the SCI, through Epidural Electrical Stimulation (EES). Such a stimulation was already tested and validated as a means of producing locomotor behaviour in otherwise paralysed limbs [2], by recruiting the neurons present in the spinal cord coherently with the spatiotemporal patterns of activation that underly a healthy subject's locomotion. Even more than reproducing locomotor behaviour, the therapy involving EES proved to provoke in the spinal cord the grey matter's plasticity in restoring cortical control below the injury [33], eventhough that is far beyond the scope of this study.
The "lower" neural network[2] can be seen as a closed-loop controller over the muscle. In reflexes for instance, no cerebral input is required to actuate the limb. Three types of neurons allow this low level communication between the CNS and the muscle. Two of which, Motor and Sensory Neurons, are now introduced. The third

[1] In the sense that it is functional, though inactive since the communication with the brain was interrupted.

[2] Below the SCI.

type, Inter-Neurons, are neurons that relay signals between the Sensory and Motor Neurons.

Motor Neurons: A Motor Neuron (MN) is a neuron whose cell body is located in the CNS, but whose axon can project outside of it to directly control effector organs, such as muscles. Each individual muscle fibre is innervated by a single MN, eventhough the latter may innervate several hundred fibres in the same muscle. Each action potential in a MN propagates along the efferent axon and gives rise to a Motor Unit action potential in the innervated muscle[3]. The Motor Unit action potentials generated by all the active MNs sum in a slightly non linear manner to produce the recordable signal called the electromyogram (EMG). EMG recordings have therefore been used as an estimate of the net instantaneous firing rate of MNs in the spinal cord [34].

Sensory Neurons: Carrying the feedback from the muscle to the CNS are the Sensory Neurons (SN). Three types of sensory feedback from the muscles are transmitted to the CNS, through afferent fibres which can be classified by the type of stimulus they primarily respond to, as is presented in Table 3.1.

Table 3.1: Types of sensory afferent fibres:

Type	Response
Ia	Changes in muscle length and contraction velocity
Ib	Changes in muscle tension
II	Position sense of a still muscle, fire when muscle is static

The arrangement of a Motor and a Sensory Neuron into a muscle-CNS closed-loop is schematized in a cross section of the spinal cord, in Figure 3.1.

The direct target of EES are not the MNs, which are after all the direct actuators of the muscles, but the SNs[4]. Indeed, excitating the sensory feedback allows to recruit the MNs indirectly through the reflex loop, which is particularly beneficial for the development of a therapy. While stimulating the firing rate of SNs, the CNS still acts as a filter for the electrical stimulation, whose stimulated area is of course far wider than that of a neuron. Targeting specific fibres or being able to track them down to the actuator would involve a much heavier development and study of the

[3] A Motor Unit (MU) is defined as a single MN and all the muscle fibres to which it connects. A single muscle is completely controlled by a group of Motor Units (MU), called a motor pool. The number of MN and of MU in a motor pool is by definition equivalent.

[4] This appears clearly when considering the fact that, in the present case, the electrode is placed on the dorsal side of the spinal cord, where SNs are (see Figure 3.1).

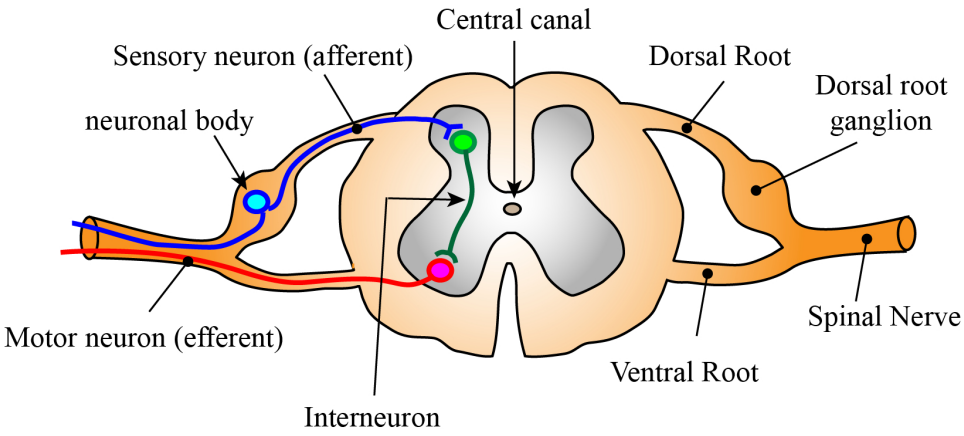

Figure 3.1: Motor and Sensory Neuron location in a spinal cord cross section. The dorsal side of the spinal cord is seen at the Figure's top. Illustration from [35].

individual's neuronal circuitry, necessary in order to stimulate directly the MNs. But instead, the filtering properties of the spinal cord will direct the sensory stimulation towards the MNs requiring excitation, while cancelling its effect onto the MNs that should remain silent. The CNS filtering furthermore allows some incertitude on the amplitude of the applied stimulation. Based on the neural architecture, a higher-amplitude stimulation would result in a higher number of MNs firing, resulting in a larger force being generated by the corresponding muscle fibres [36]. Finally, a capital asset of targeting the SNs is that their stimulation -within reasonable amplitudes- is not sufficient to produce motor behaviour on its own. The patient's motion is therefore restricted to the voluntary actuation of his own limbs: only when both the stimulation and the patient's intentions coincide the motion is produced. And as such EES favours the growth of new relay circuits down the spinal cord [33]!
However at the time of this study it is not yet possible to record the neural activity in real time during normal behaviour [36], and as such neuro-musculoskeletal models are used to predict natural spatiotemporal patterns of the proprioceptive feedback. In-depth knowledge of sensory fibres' activity during movement is critical to understand the interaction of EES with the sensorimotor circuitry controlling movement, which is a prerequisite to develop efficient therapeutic stimulation strategies.

Motor pools of NHP arm muscles

Physiologically, a single muscle is controlled by a group of Motor Units, called a motor pool. It is to be noted that the motor pool's cardinality correlates with the muscle's size, and its position in the spinal cord (see Figure 1.2) correlates with the mechanical action with which the muscle is associated [34]. The spatial distribution of motor pools of 11 NHP arm muscles [8], spanning the spinal cord from the

C4 to the T2 segment, are reported in Table 3.2 and Table 3.3. One can observe the imbalance occurring between counts of flexor and extensor MNs, imbalance which was expected from previous studies [34]. An important assumption underlying the presentation of this data is that the SN distribution resembles the MN distribution in the spinal cord, assumption which may appear reasonable when considering the natural arrangements schematized in Figure 3.1. While the correspondence in numbers is by no means guaranteed, the proportional distribution of SNs probably resembles the MNs' due to the energy cost of connecting fibres relatively distant from one another during the body's development. To our knowledge, anatomical studies also focused on counting MNs, and not SNs.

Table 3.2: Size of the motor pools reported for the NHP [8]:

Muscle	Count []	Muscle	Count []
biceps	1051	triceps	1271
flex_carpi_radialis	235	ext_carpi_radialis	890
flex_carpi_ulnaris	314	ext_carpi_ulnaris	216
abd_poll_longus	126	flex_digit_superficialis	306
ext_digitorum	273	flex_digit_profundus	475
ext_digiti	87		

Modelling

In order to characterize spatiotemporal patterns of sensory activity through the spinal cord, a neuronal model is coupled with the musculoskeletal model described in the previous Chapter. Unfortunately for the modeller it appears clearly from the data (see Table 3.2) that it becomes technically difficult to predict individually the firing rate of every SN of every muscle [7]. However, combining neural control signals and musculoskeletal models remains vital to resemble closely the biological closed-loop process [36].
The decision can then be to either reduce the complexity of the musculoskeletal model [36], or to reduce the complexity of the neuronal model [2]. In the present study given the aim of restoring a three-dimensional, multi-joint motor behaviour, the choice was to consider homogeneous the spatiotemporal activation of selected ensembles of a muscle's SNs. The simplest SN ensemble to consider corresponds to a single muscle's sensory fibres pool. The sensory feedback is then approximated at the simplest level recognized as effective [2]: as a single one-dimensional scalar per muscle's afferent fibre type.

3.2 Prochazka's model

Ensemble firing profiles of muscle afferents, measured in cats during normal stepping [37], are approximated by simple yet reasonably accurate and widely echoed ([36][38][39][40]) polynomial functions [1].

Ia afferents:

Ia fibres convey the state of the muscle spindles' stretching to the CNS [1]. It has been noted that the most important contribution to their firing frequency is the fibre contraction velocity v^M [37]. The model was furthermore slightly improved by the addition of a term able to carry bursts in muscle activity, as an approximation of the α-γ linkage [39]. The Ia firing rate of a single MTU is computed as

$$f_{\text{Ia}} = k_v sign\left(v^M\right)\left|v^M\right|^{p_v} + k_{dI}\left(l^M - l^M_{opt}\right) + k_{nI}a + const_I. \tag{3.1}$$

Beyond the fibre velocity v^M [mm/s], the individual muscle's contribution to the equation includes the fibre length l^M [mm], the optimal fibre length l^M_{opt} [mm], and the normalized activity a []. The parameters of this equation are retrieved from the study of cat normal locomotion [1], until more measurements are made in the NHP, namely, $k_v = 4.3$, $p_v = 0.6$, $k_{dI} = 2$, $k_{nI} = 50$, and $const_I = 20$.

Ib afferents:

Ib fibres transmit the state of Golgi tendon organs to the CNS [1]. Their firing rate is computed as

$$f_{\text{Ib}} = k_F \frac{F^M}{F^M_{max}}, \tag{3.2}$$

where the fibre force F^M [N] and the maximal isometric force F^M_{max} [N] are taken into account, and the parameter $k_F = 333$ is used [1].

II afferents:

Secondary fibres transmit the muscle spindles' state to the CNS [1], but unlike primary Ia fibres, they do not carry information on the contraction velocity. Therefore, they only update the fibre's instantaneous stretching for the CNS. However, as for the Ia fibres, the model includes a term in muscle activity accounting for the α-γ linkage, eventhough the gain constant of this term is expected to be relatively smaller to that of the primary fibres [1]. Their firing rate is finally computed as

$$f_{\text{II}} = k_{dII}\left(l^M - l^M_{opt}\right) + k_{nII}a + const_{II}, \tag{3.3}$$

where the fibre length l^M [mm], the optimal fibre length l^M_{opt} [mm], and the muscle's normalized activation a [] are used. The parameters are those of the cat's normal locomotion [1], i.e. $k_{dII} = 13.5$, $k_{nII} = 20 \leq k_{nI}$ and $const_{II} = const_I = 10$.

Table 3.3: Motor Neuron proportional distribution in the spinal cord segments [8]: *In humans, it was observed that the deltoid's MN distribution was quite similar to the biceps. Hence the distribution of the biceps MNs is taken as the deltoid's, eventhough it was not measured in NHP.

	deltoid*	biceps	triceps	flex_carpi_radialis
C4				
C5	0.2016	0.2016	0.0054	
C6	0.4651	0.4651	0.0475	
C7	0.2523	0.2523	0.2608	0.7647
C8	0.0808	0.0808	0.5331	0.2164
T1			0.1498	0.0189
T2			0.0033	
	ext_carpi_radialis	flex_carpi_ulnaris	ext_carpi_ulnaris	abd_poll_longus
C4	0.0042			
C5	0.1446			
C6	0.5688		0.0197	
C7	0.2307	0.0359	0.0466	0.0237
C8	0.0429	0.7122	0.5219	0.3855
T1	0.0088	0.2519	0.4118	0.5907
T2				
	flex_digit_superficialis	ext_digitorum	flex_digit_profundus	ext_digiti
C4				
C5				
C6				
C7		0.0325	0.0216	
C8	0.2614	0.6519	0.4395	0.3128
T1	0.7329	0.3156	0.5081	0.6492
T2	0.0056		0.0308	0.0379

Lower limit

Each computed firing rate is constrained to be positive, such that

$$f = \max(f, 0), \tag{3.4}$$

where f is either one of f_{Ia}, f_{Ib} or f_{II}.

Neuronal activity by spinal segment

Firing profiles of the studied muscles are eventually combined to predict the global activity profile by spinal segment (see Figure 1.2). The cardinality of the motor pools (see Table 3.2) is however not taken into account, as the contribution of larger muscles to the global profile would overshadow the contribution of smaller muscles. When this choice distances the predictions made with the model from the reality, it appears necessary to be able to visualize patterns of activation produced by small amplitude movements. Furthermore, the assumption was made that the distribution of the SNs matches the distribution of MNs in the spinal cord, but the absolute numbers could be different. Therefore, the neuronal activity a^i of fibres f, predicted for the i^{th} spinal segment is

$$a^i = \frac{\sum_{j=0}^{N_{mtu}} \omega_j^i f_j}{\sum_{j=0}^{N_{mtu}} \omega_j^i}, \tag{3.5}$$

where f_j is the firing rate of either type of fibre computed for muscle j, and ω_j^i is the proportion of muscle j's motor pool found in the i^{th} spinal segment. For muscles whose MN distribution is not reported in Table 3.3, the distribution is taken by default as identically null across the spinal cord. Finally given the small proportional presence of MNs in segments C4 and T2, it is decided to not consider these segments until more data are collected.

3.3 Results

Predictions of neuronal activity underlying the NHP's reaching and grasping task are made. The 4.5 s long task involved significant evolutions in the θ_S^a, θ_S^f, θ_E^f and θ^p joint angles, as is seen in Figure 3.2.
It is divided into four phases, in order; preparation, reaching, grasping and returning [4]. The wrist DoF are locked, since the marker placement (see Figure 2.8) does not allow to monitor them. However their variation is expected to be small as the grasping phase, which requires the animal to close his hand around a handle, primarily involves DoFs around the fingers, which are not presently modelled anyway. Other phases mainly involve the shoulder and elbow joints, with the wrist joints being used to fine tune the hand's position. Muscle activity as well as fibre length, velocity, and force, outputs of the computations performed on the musculoskeletal

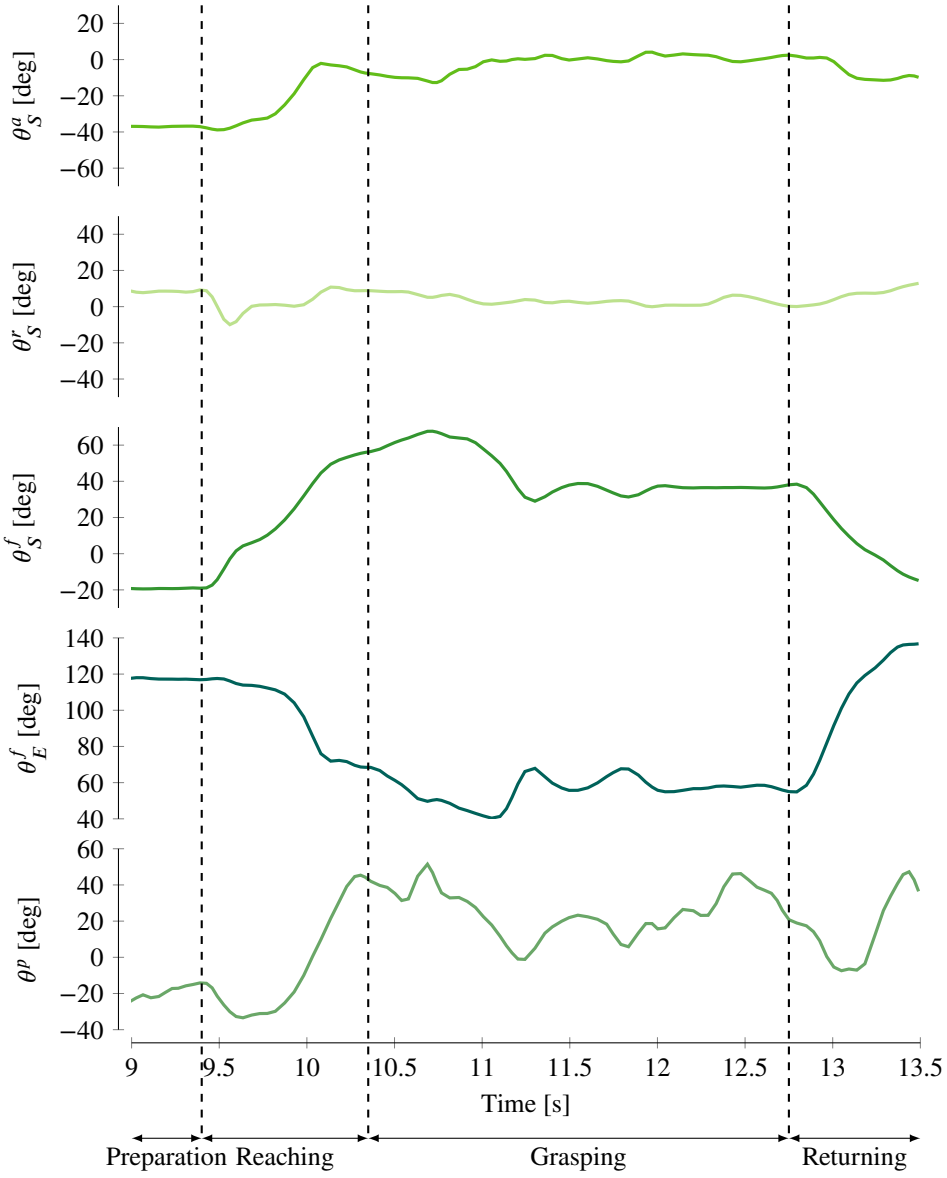

Figure 3.2: Joint angle evolution during a reaching and grasping task. The motion can be divided into four characteristic phases: preparation, reaching, grasping and returning.

model, are filtered with a first order adaptive filter (filtfilt), of Nyquist frequency $W_N = 0.001$ [].

3.3.1 Muscle afferent firing rate

The macroscopic pattern of sensory activity computed in equation (3.5) gives valuable insight at the cost of losing individual muscle response, as well as dimensional meaningfulness, since averaging frequencies does not necessarily yield a frequency[5]. Therefore as a preamble the afferent activities computed for muscles that are of capital importance during the task are presented. The deltoid for the shoulder joints, the biceps and the triceps[6] for the elbow joint, as presented in Figure 3.3. One observes the clear phase opposition between the biceps and the triceps responses, as well as the continuous importance of the deltoid to maintain the shoulder at an angle throughout the recording (the subject is raising the arm, therefore the deltoid is under tension for most of the task). We notice that the half time in phases involving high amplitude movements (i.e. reaching and returning) corresponds not to the peaks of sensory feedback, but rather to the half point transition between two extremal values.

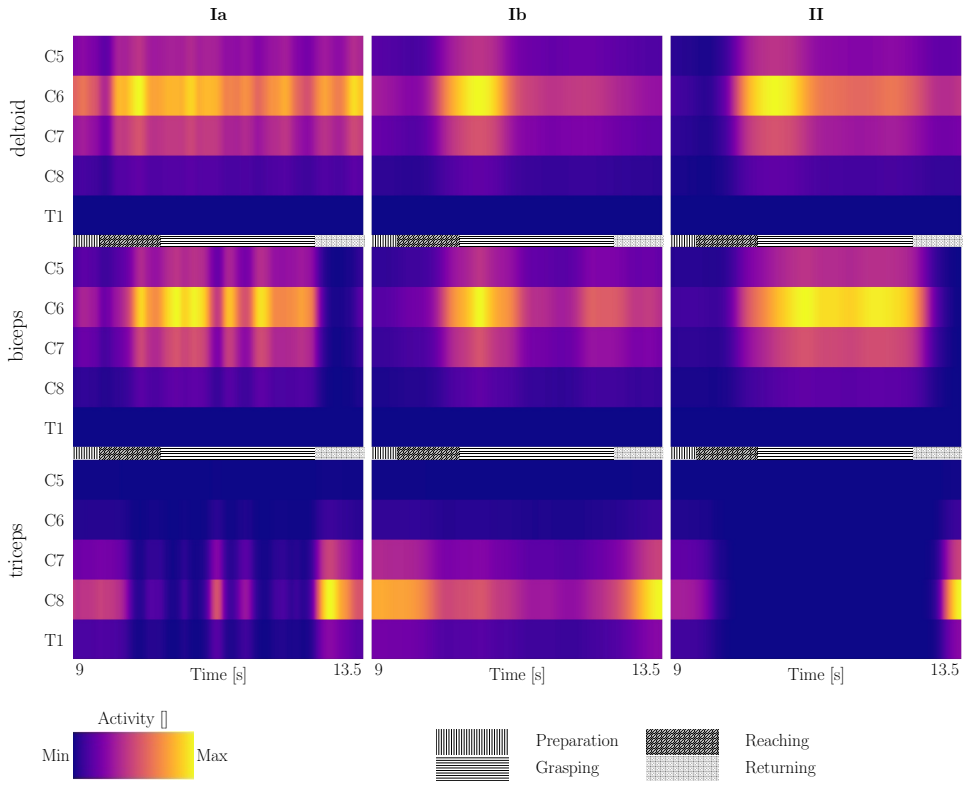

Figure 3.3: Sensory feedback throughout the spine in the reaching and grasping task, singled out for three muscles of the arm acting primarily on the shoulder and elbow flexion.

[5]For instance, two signals oscillating at 100 Hz in phase opposition would have an "average" frequency of 100 Hz, while the observed signal would oscillate at 200 Hz.

[6]All of whose different heads' firing rates are being averaged.

Furthermore we notice in the motor pool distribution that the extensor carpi ulnaris muscle shares with the biceps a similar motor pool distribution. Therefore we wondered what would be the activity patterns of this muscle, and wanted to gain some hindsight before averaging the sensory feedbacks by spinal segment. The C6 average activity will be mostly affected by the deltoid, biceps, and extensor carpi ulnaris muscles as can be seen in Table 3.3. The afferent activity of the extensor carpi ulnaris and its antagonist muscle, the flexor carpi ulnaris, are presented in Figure 3.4. We notice that at the first order (II-type fibres), the response of both these muscles follow that of the biceps. This is because they both originate at the lower head of the humerus and the elbow flexion directly affects their length, although they cannot produce large torques for the elbow flexion. Considering that the same response will be observed for several muscles of the forearm (attached to the lower head of the humerus), we expect that in the global activity patterns, the phase opposition that we could observe between the triceps and biceps response will be drown under the homogeneous activity patterns of forearm muscles, which again will be passive actuators until more degrees of freedom are added to the model.

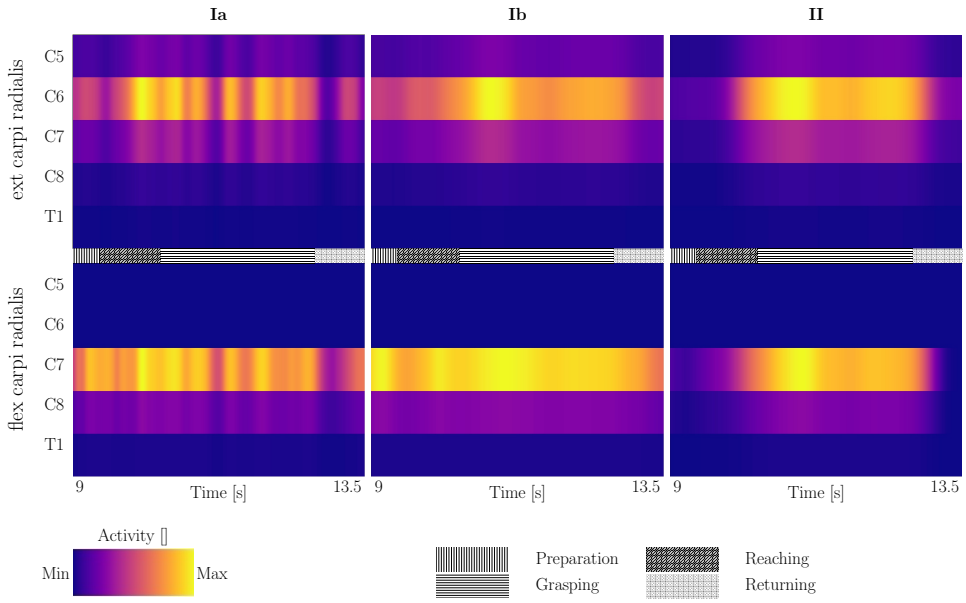

Figure 3.4: Sensory feedback throughout the spine in the reaching and grasping task, singled out for two muscles of the forearm, actuators of joints which are not modelled. However since they originate at the lower end of the humerus, their length is constrained by the elbow flexion and the sensory response is observable.

3.3.2 Macroscopic patterns of sensory neuronal activity

From equation (3.5) we can withdraw an estimation of the global activity for each afferent fibre type in each spinal segment, at time t, presented in Figure 3.5. Com-

pared to the results previously obtained for singled-out muscles, one notices two major pattern differences. First the grasping phase, characterized by a flexed elbow and an extended shoulder, coincides with stronger activities in both the C5 and the C6 segments of the spinal cord, with a gradual decrease in the lower segments. This differs with the peak of sensory activity seen in the lone C6 segment that was observed for the singled-out deltoid and biceps muscles. Then, the returning phase is not explicitly visible: the activation in lower segments, that was evident for the triceps muscle, is absent from the map. This is likely to be explained by the contribution to the lower segments' averages of a number of forearm muscles whose sensory feedback can effectively shade the single triceps'.
Furthermore, it is interesting to see that the difference between Ia and II-type fibres firing rates is accentuated in the global pattern. Recall that (equation (3.1) and equation (3.3)) the difference between those two sensory feedbacks primarily comes from the term in contraction velocity influencing the firing rate of Ia fibres[7]. In the present case, this coincides with amplitude peaks in the macroscopic activity. Interestingly, the resurgence in elbow flexion occurring between 11 and 12 s (Ia activity, two darker vertical lines mid experiment, corresponding to two peaks in θ_E^f as in Figure 3.2) is more visible on the global pattern than on the firing rate of biceps afferents.

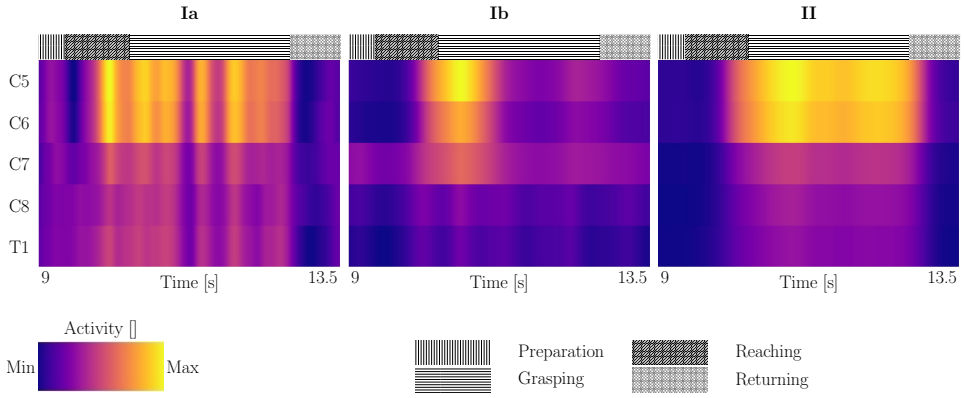

Figure 3.5: Macroscopic afferent activity, computed for the three types of afferent fibres in the reaching and grasping task.

Importance of the EMG-related term in Ia and II firing rates

The noisy nature of the Ia afferent response made us question the importance of the term in muscle activation in the computation of the muscles' firing rates. This second order term improved the predictions obtained in the study of cat normal gait [1], and allegedly represents the α-γ MN co-activation. Figure 3.6 shows the predictions obtained with Prochazka's model not considering a term in muscle activation,

[7] As a matter of fact, the Ia response is primarily shaped by the contraction velocity.

$k_{nI} = k_{nII} = 0$.

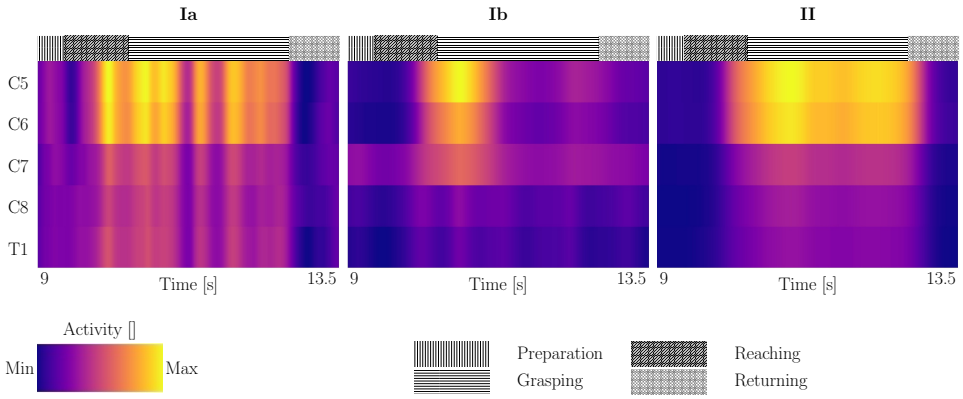

Figure 3.6: Macroscopic afferent activity, computed for the three types of afferent fibres in the reaching and grasping task, for $k_{nI} = k_{nII} = 0$.

The light difference observed with Figure 3.5 confirmed that the importance of the EMG-estimate term, relative to the fibre contraction velocity and length, is small as it should be [1]. The noisy nature of contraction velocities, before and after filtering, is presented in Figure 3.7 for two MTUs of the modelled arm (the long heads of the biceps and triceps).

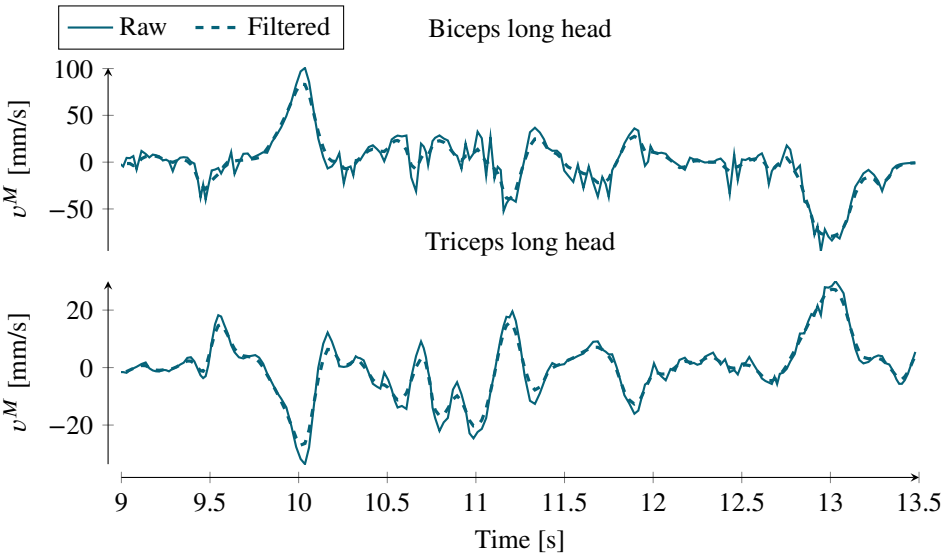

Figure 3.7: Fibre contraction velocities of the biceps and triceps long heads during the reaching and grasping task, before and after filtering.

Chapter 4 Discussion

As is the case with every model, the assumptions and simplifications constitute the limits of the prediction capabilities. In this Chapter different stages of the model's development are discussed, as well as the obtained results and some ideas to further development.

Skeletal model

Simplifications made at the first stage of modelisation have an undetermined impact throughout development. For instance the idea of idealised, decoupled joint angles will certainly affect the entirety of results, but simply quantifying the impact on the final result is not trivial. As a general note, it is expected based on previous comparisons [14] that the more physiologically correct the model, the better the predictions can be. However in the present case, improving the joint modelisation would call for physiologist-specific skills and knowledge, and it is therefore a minor concern for us as it requires the involvement of additional people. After all, the development and validation of physiologically precise musculoskeletal models is usually left to multidisciplinary teams that work extensively on it: there are only two complete OpenSim models of the human lower limb, one being a simplification of the other (54 MTUs instead of 92), eventhough the study of human gait is the software's first objective.
However if more time was to be dedicated on this primate arm model, it seems feasible to add in it the scapular translation, which would increase the range of shoulder motion in which MTUs are not unrealistically constrained. But this would first require to non invasively measure the actual scapular translation occurring during a real movement[1].
Furthermore, one could decide to add a finger joint in order to observe on the spinal maps a proper migration of the afferent activities towards the lower portions of the spinal cord. Indeed, the motor pool distributions showed that these lower segments hold most of the finger actuator MNs. The computational cost of modelling all finger joints is probably too high[2] for the study of the reaching and grasping task. However, it was at one point proposed to add a single uniform flexion joint around

[1] Without the means to do this, previous teams palpated the NHP's scapula during motion to estimate the model's validity limits [5].

[2] After all, specific models are developed for the study of grasping specifically [11]. But such models are rather weak around the shoulder, which is problematic for the three dimensional task.

the first phalanx, spanning four fingers (excluding the thumb). Under the assumption that these fingers' motion is synchronized (the NHP grasps the handle with the entire hand), this could dramatically improve the precision of the spatiotemporal patterns of sensory activity.

Muscular model

The precision with which to model the MTUs can be arbitrarily high: given the number of parameters it has been argued that even the more advanced models would represent nothing more than a curve fitting exercise without physiological basis [14]! Yet our model could be simpler. An approximation, that was not made in the current model, would have been to group the actuators by function. For instance, the brachialis and biceps short head have similar paths and purposes in flexing the elbow. It is common in musculoskeletal modelling to group such similar actuators into one stronger but single actuator, on either the PCSA [14] or the moment arm [41]. The validity of such an approximation can only be reduced to the variety of patterns of sensory activations which are expected to be visible on the final spinal maps. In the present case, it could appear as a reasonable option[3], eventhough the physiological precision would suffer a lot as it would not be possible to directly validate or invalidate a MTU with NHP morphometrical data. It is also unclear how impactful such an approximation would be in the reproduction of original kinematics. For instance, in NHP there is no one to one correspondence between individual fingers and forearm muscles. Therefore moving any single digit alone requires coordinating the activity of several muscles, that have mechanical actions on many digits [26].
To improve the present model, more accurate data could be collected so that the operating range width of MTUs remains closer to 1 (in units of normalized length[4]). This would improve the realistic force generation capabilities of each MTU, but would require an intense effort and study of attachment points, lines of action (therefore including wrapping surfaces, which will significantly increase computational cost once they are added), and of course parameters such as the optimal fibre length and the tendon slack length.
On the validation of the muscular model, one should take into account that the moment arms have been observed to vary by a factor of two between individuals [23], and it is therefore impossible to expect identical recruiting between the model and the recorded EMGs. The activation patterns themselves, even between comparably sized subjects, was observed as very different [14].
Beyond that, we recall that the activation of a muscle[5] is not instantaneous [17]

[3] As long as it would be restricted to grouping MTUs whose shortening or lengthening are similar in all motions studied, given Prochazka's model. This would englobe forearm muscles and some elbow actuators, but probably not many shoulder actuators.

[4] Extensive work was made on this model to keep the normalized lengths in plausible ranges: above 0.6 and below 1.4. Originally the passive forces produced by overstretched muscles seriously hindered the model's ability to reproduce any motion at all.

[5] It was however measured as similar across all human muscles of mixed fibre type [19].

and also subject-specific. The study of athletes' biomechanics by Prof. Nakamura (University of Tokyo), showed that the athletes' muscles had typically shorter activation times than those of normal people. The extensive training athletes went through also allowed them to actuate less muscles non critical to the motion. Such considerations could eventually be considered in models developed for the study of subjects with partial disabilities, and therefore specific muscle constraints.

Neuronal model

Spinal maps obtained suffer a lot from the precision with which the motor pools distributions are known. First by the discretization of the spinal cord: considering spinal segments as uniform seems rough (Yakovenko [34] used at least three sub-segments to produce the original spinal maps), and more precise patterns of activation could be observed. Second by the number of muscles whose motor pool is documented. Without hindsight on the distribution of the shoulder muscles' motor pools in the NHP (the only one considered is the deltoid, which was assumed to have a similar motor pool distribution than that of the biceps), it is indeed impossible to observe patterns of activation corresponding to the shoulder motion. The next efforts made on the neuronal model should therefore be to obtain this data, after which it would be beneficial to tune the parameters of Prochazka's model following the study of the NHP's reaching and grasping task.
Furthermore it is unclear whether the current model can reflect the recruitment principle[6], that models emphasizing the neuronal aspect instead of the musculoskeletal aspect encoded [7].

Reaching and grasping task

Finally the experimental task has an importance on the end result: we expect to obtain greatly stereotyped neuronal firing patterns by recording the reaching kinematics in a limited space[7], but it would be interesting to quantify the coupling of muscle activations or their relative importance to the motion. In that endeavour, the musculoskeletal model could also be used as a tool to design neurophysiological experiments [5]. Furthermore force measurements, performed on the handle the NHP is grasping, could be taken into account to predict muscle contractions.

[6] It states that for a given recruitment (force) level, smaller MNs fire before larger ones.

[7] And with the primate's torso being fixed in place by plexiglas plates, which have been added in Fribourg's experimental setup after the collection of the kinematics considered for this report.

Bibliography

[1] A. Prochazka, "Quantifying proprioception," *Progress in brain research*, vol. 123, pp. 133–142, 1999.

[2] M. Capogrosso, T. Milekovic, D. Borton, F. Wagner, E. M. Moraud, J.-B. Mignardot, N. Buse, J. Gandar, Q. Barraud, D. Xing *et al.*, "A brain–spinal interface alleviating gait deficits after spinal cord injury in primates," *Nature*, vol. 539, no. 7628, p. 284, 2016.

[3] "Novel neuro-stimulation therapy for spinal cord injury: G-therapeutics raises $36 millions to develop novel neuro-stimulation therapy for spinal cord injury," *Press article*, 2016.

[4] L. Miller, P. Van Kan, T. Sinkjær, T. Andersen, G. Harris, and J. Houk, "Correlation of primate red nucleus discharge with muscle activity during free-form arm movements." *The Journal of Physiology*, vol. 469, no. 1, pp. 213–243, 1993.

[5] S. S. Chan and D. W. Moran, "Computational model of a primate arm: from hand position to joint angles, joint torques and muscle forces," *Journal of neural engineering*, vol. 3, no. 4, p. 327, 2006.

[6] S. L. Delp, F. C. Anderson, A. S. Arnold, P. Loan, A. Habib, C. T. John, E. Guendelman, and D. G. Thelen, "Opensim: open-source software to create and analyze dynamic simulations of movement," *IEEE transactions on biomedical engineering*, vol. 54, no. 11, pp. 1940–1950, 2007.

[7] M. Sreenivasa, A. Murai, and Y. Nakamura, "Modeling and identification of the human arm stretch reflex using a realistic spiking neural network and musculoskeletal model," in *Intelligent Robots and Systems (IROS), 2013 IEEE/RSJ International Conference on*. IEEE, 2013, pp. 329–334.

[8] A. Jenny and J. Inukai, "Principles of motor organization of the monkey cervical spinal cord," *Journal of Neuroscience*, vol. 3, no. 3, pp. 567–575, 1983.

[9] M. Godschalk, R. N. Lemon, H. G. Kuypers, and H. Ronday, "Cortical afferents and efferents of monkey postarcuate area: an anatomical and electrophysiological study," *Experimental Brain Research*, vol. 56, no. 3, pp. 410–424, 1984.

[10] G. L. Gottlieb, Q. Song, G. L. Almeida, D.-A. Hong, and D. Corcos, "Directional control of planar human arm movement," *Journal of Neurophysiology*, vol. 78, no. 6, pp. 2985–2998, 1997.

[11] S. Schaffelhofer, M. Sartori, H. Scherberger, and D. Farina, "Musculoskeletal representation of a large repertoire of hand grasping actions in primates," *IEEE Transactions on Neural Systems and Rehabilitation Engineering*, vol. 23, no. 2, pp. 210–220, 2015.

[12] K. M. Graham and S. H. Scott, "Morphometry of macaca mulatta forelimb. iii. moment arm of shoulder and elbow muscles," *Journal of morphology*, vol. 255, no. 3, pp. 301–314, 2003.

[13] F. Khali, "Reduire, raffiner, remplacer: questions to professor rouiller, president of the medicine faculty and comitee member of the swiss primate competence center for research," https://www.unifr.ch/neuro/rouiller/assets/files/presse/ufjuin54-562.pdf, 2013, accessed: 2018-01-12.

[14] D. G. Lloyd and T. F. Besier, "An emg-driven musculoskeletal model to estimate muscle forces and knee joint moments in vivo," *Journal of biomechanics*, vol. 36, no. 6, pp. 765–776, 2003.

[15] E. J. Cheng and S. H. Scott, "Morphometry of macaca mulatta forelimb. i. shoulder and elbow muscles and segment inertial parameters," *Journal of Morphology*, vol. 245, no. 3, pp. 206–224, 2000.

[16] K. R. Saul, X. Hu, C. M. Goehler, M. E. Vidt, M. Daly, A. Velisar, and W. M. Murray, "Benchmarking of dynamic simulation predictions in two software platforms using an upper limb musculoskeletal model," *Computer methods in biomechanics and biomedical engineering*, vol. 18, no. 13, pp. 1445–1458, 2015.

[17] G. T. Yamaguchi, D. W. Moran, and J. Si, "A computationally efficient method for solving the redundant problem in biomechanics," *Journal of Biomechanics*, vol. 28, no. 8, pp. 999–1005, 1995.

[18] D. G. Thelen *et al.*, "Adjustment of muscle mechanics model parameters to simulate dynamic contractions in older adults," *Transactions-American Society Of Mechanical Engineers Journal Of Biomechanical Engineering*, vol. 125, no. 1, pp. 70–77, 2003.

[19] L. M. Schutte, M. M. Rodgers, F. Zajac, and R. M. Glaser, "Improving the efficacy of electrical stimulation-induced leg cycle ergometry: an analysis based on a dynamic musculoskeletal model," *IEEE Transactions on Rehabilitation Engineering*, vol. 1, no. 2, pp. 109–125, 1993.

[20] M. Millard, T. Uchida, A. Seth, and S. L. Delp, "Flexing computational muscle: modeling and simulation of musculotendon dynamics," *Journal of biomechanical engineering*, vol. 135, no. 2, p. 021005, 2013.

[21] M. Millard, "Muscle models in opensim 3.0 - theory and application," https://www.youtube.com/watch?v=Q1rId1fOkjw, 2013, accessed: 2018-11-27.

[22] J. T. Chand, "Complete description of the thelen2003muscle model," *OpenSim documentation*.

[23] J. L. Hicks, T. K. Uchida, A. Seth, A. Rajagopal, and S. L. Delp, "Is my model good enough? best practices for verification and validation of musculoskeletal models and simulations of movement," *Journal of biomechanical engineering*, vol. 137, no. 2, p. 020905, 2015.

[24] J. P. Charles, O. Cappellari, A. J. Spence, D. J. Wells, and J. R. Hutchinson, "Muscle moment arms and sensitivity analysis of a mouse hindlimb musculoskeletal model," *Journal of anatomy*, vol. 229, no. 4, pp. 514–535, 2016.

[25] W. E. Edwards, "Study of monkey, ape, and human morphology and physiology relating to strength and endurance, phase iv. the musculoskeletal anatomy of the thorax and brachium of an adult female chimpazee," 6571st Aeromedical Research Laboratory, Aerospace Medical Division, Air Force Systems Command, Holloman Air Force Base, New Mexico, Tech. Rep., 1965.

[26] P. L. Gribble and D. J. Ostry, "Compensation for interaction torques during single-and multijoint limb movement," *Journal of neurophysiology*, vol. 82, no. 5, pp. 2310–2326, 1999.

[27] F. C. Anderson and M. G. Pandy, "Static and dynamic optimization solutions for gait are practically equivalent," *Journal of biomechanics*, vol. 34, no. 2, pp. 153–161, 2001.

[28] D. A. Kistemaker, J. D. Wong, and P. L. Gribble, "The central nervous system does not minimize energy cost in arm movements," *Journal of neurophysiology*, vol. 104, no. 6, pp. 2985–2994, 2010.

[29] F. Dzeladini, J. Van Den Kieboom, and A. Ijspeert, "The contribution of a central pattern generator in a reflex-based neuromuscular model," *Frontiers in human neuroscience*, vol. 8, 2014.

[30] M. V. Liarokapis, P. K. Artemiadis, P. T. Katsiaris, K. J. Kyriakopoulos, and E. S. Manolakos, "Learning human reach-to-grasp strategies: Towards emg-based control of robotic arm-hand systems," in *Robotics and Automation (ICRA), 2012 IEEE International Conference on*. IEEE, 2012, pp. 2287–2292.

[31] R. S. Maeda, T. Cluff, P. L. Gribble, and J. A. Pruszynski, "Compensating for intersegmental dynamics across the shoulder, elbow and wrist joints during feedforward and feedback control," *bioRxiv*, p. 115675, 2017.

[32] M. Boots, A. Sobinov, V. Gritsenko, M. Mansouri, L. E. Fisher, J. L. Collinger, R. A. Gaunt, and S. Yakovenko, "Scaling of musculoskeletal morphometry for human upper-limb models," 2017, sfN Society for Neuroscience. [Online]. Available: http://www.abstractsonline.com/pp8/#!/4376/presentation/12741

[33] G. Courtine, "Ted talk: the paralyzed rat that walked," https://www.youtube.com/watch?v=X9FFzWUInyA, 2014, accessed: 2018-01-16.

[34] S. Yakovenko, V. Mushahwar, V. VanderHorst, G. Holstege, and A. Prochazka, "Spatiotemporal activation of lumbosacral motoneurons in the locomotor step cycle," *Journal of neurophysiology*, vol. 87, no. 3, pp. 1542–1553, 2002.

[35] "Chapter 2: the spinal cord," http://neurones.co.uk/Neurosciences/Chapters/Chapter 202/A.2.1 20Spinal 20Cord.html , accessed: 2018-01-12.

[36] M. Sreenivasa, K. Ayusawa, and Y. Nakamura, "Modeling and identification of a realistic spiking neural network and musculoskeletal model of the human arm, and an application to the stretch reflex," *IEEE Transactions on Neural Systems and Rehabilitation Engineering*, vol. 24, no. 5, pp. 591–602, 2016.

[37] A. Prochazka and M. Gorassini, "Models of ensemble firing of muscle spindle afferents recorded during normal locomotion in cats," *The Journal of physiology*, vol. 507, no. 1, pp. 277–291, 1998.

[38] S. N. Markin, A. N. Klishko, N. A. Shevtsova, M. A. Lemay, B. I. Prilutsky, and I. A. Rybak, "Afferent control of locomotor cpg: insights from a simple neuromechanical model," *Annals of the New York Academy of Sciences*, vol. 1198, no. 1, pp. 21–34, 2010.

[39] E. M. Moraud, M. Capogrosso, E. Formento, N. Wenger, J. DiGiovanna, G. Courtine, and S. Micera, "Mechanisms underlying the neuromodulation of spinal circuits for correcting gait and balance deficits after spinal cord injury," *Neuron*, vol. 89, no. 4, pp. 814–828, 2016.

[40] S. Gervasio, M. Voigt, U. G. Kersting, D. Farina, T. Sinkjær, and N. Mrachacz-Kersting, "Sensory feedback in interlimb coordination: Contralateral afferent contribution to the short-latency crossed response during human walking," *PloS one*, vol. 12, no. 1, p. e0168557, 2017.

[41] N. Van der Noot, "Hill muscles characterisation," *Biorob internal*, 2015.

[42] L. Zhou, Y. Li, and S. Bai, "A human-centered design optimization approach for robotic exoskeletons through biomechanical simulation," *Robotics and Autonomous Systems*, vol. 91, pp. 337–347, 2017.

[43] A. Cappozzo, F. Catani, U. Della Croce, and A. Leardini, "Position and orientation in space of bones during movement: anatomical frame definition and determination," *Clinical biomechanics*, vol. 10, no. 4, pp. 171–178, 1995.

[44] W. Maurel, "3d modeling of the human upper limb including the biomechanics of joints, muscles and soft tissues," Ph.D. dissertation, EPFL, 1999.

[45] S. A. Schloemer, E. J. Caruthers, R. K. Baker, N. C. Pelz, A. M. Chaudhari, and R. A. Siston, "Static optimization vs. computed muscle control characterizations of neuromuscular control: Clinically meaningful differences?" *Conference: Biomechanics and Neural Control of Movement*, 2016.

[46] M. I. Christel and A. Billard, "Comparison between macaques and humans kinematics of prehension: the role of morphological differences and control mechanisms," *Behavioural brain research*, vol. 131, no. 1, pp. 169–184, 2002.

[47] K. Singh, E. H. Melis, F. J. Richmond, and S. H. Scott, "Morphometry of macaca mulatta forelimb. ii. fiber-type composition in shoulder and elbow muscles," *Journal of morphology*, vol. 251, no. 3, pp. 323–332, 2002.

[48] T. Brochier, R. L. Spinks, M. A. Umilta, and R. N. Lemon, "Patterns of muscle activity underlying object-specific grasp by the macaque monkey," *Journal of neurophysiology*, vol. 92, no. 3, pp. 1770–1782, 2004.

[49] M. A. Sherman, A. Seth, and S. L. Delp, "What is a moment arm? calculating muscle effectiveness in biomechanical models using generalized coordinates," in *Proceedings of the... ASME Design Engineering Technical Conferences. ASME Design Engineering Technical Conferences*. NIH Public Access, 2013.

Appendices

Appendix A Differences between human and NHP arms

A.1 Skeleton

The arm's bones are only slightly different: the macaque's humerus presents a slight bending, while the human one is straight. However the NHP's scapula is different than that of humans' in both size and orientation [46]. In the NHP the scapula is wider, and is oriented largely in the sagittal plane relative to the rib cage. Whereas in humans, the scapula is diagonal and posterolateral to the rib cage [12].
The models' humerus, ulna, radius, scapula and clavicula were scanned from a representative rhesus macaque of 7.5kg. However the hand and wrist bones could not be digitized, and scaled down scans of the humans' hand and wrist are used [5].

A.2 Musculo-tendon complex

The NHP has an additional muscle compared to humans: the dorsoepitrochlearis, a climbing muscle that has been assumed to be either part of the tricep or the lattissimus dorsi complex [25]. Factually, it originates from the lattissimus dorsi and inserts onto the triceps brachii tendon on the medial aspect of the elbow [12], as presented in Figure A.1. Its role is to adduct the upper arm [46].
Otherwise the muscles Physiological Cross-Sectional Area (PCSA) -observation of the muscle fibre count- are similar in humans and in macaques, despite the two species disparity in size and weight [46]. This of course results in greater relative muscle forces in the NHP. In humans, the greater dimensions seem to increase the muscle's torques enough to move heavier limbs [12].

A.3 Usage and limitations

The macaques' scapula being more horizontal implies that the shoulder rotation is more restricted than it is for humans [46]. Unlike humans, macaques are not able to fully extend the elbow into a straight arm position [5]. However the wrist is more flexible in NHP: it can flex and adduct more than in humans [11]. The arm's DoF boundaries are presented in Table A.1.

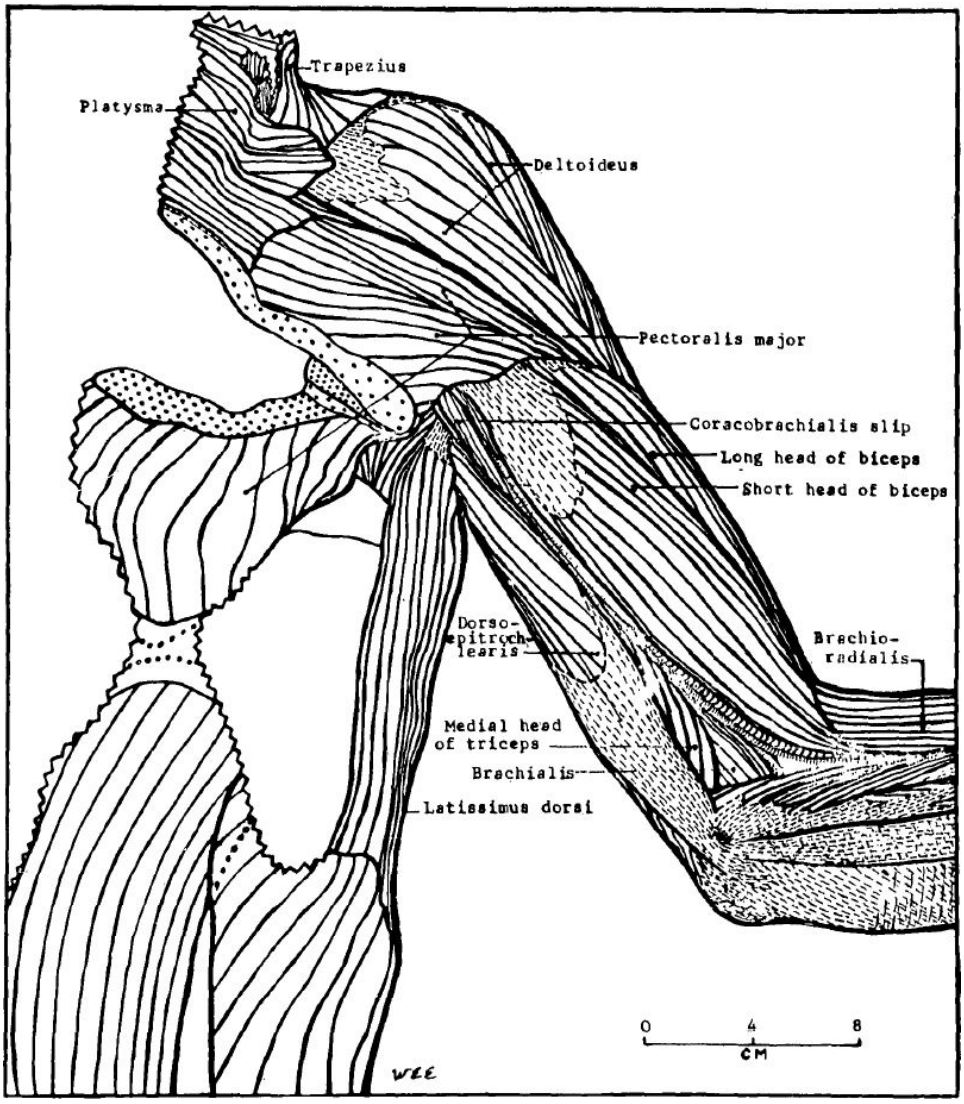

Figure A.1: Illustration of the macaque's arm anatomy [25], highlighting the situation of the dorsoepitrochlearis muscle (centered).

In the live animal, the scapula can move in what is called the scapular translation. While it is an important part of the musculoskeletal model as some muscles are attached to the scapula, it cannot currently be implemented in the model due to a lack of measurements. Quantifying the scapular translation indeed requires to be able to measure its displacement non-invasively in live animals, which to our knowledge has not been made for the NHP yet.
Qualitatively, it becomes significant when the NHP arm evolves above the eyes (shoulder abducted by 90 degrees). In humans it is more critical for both the shoulder abduction and rotation: from external shoulder rotations above 15 degrees, or

Table A.1: Observed limits of the joint angles (in degrees) in humans and macaques (these angles are illustrated in Figure 2.2):

Joint angle	Notation	Macaque [5]	Human [16]
Shoulder adduction	θ^a_S	$[-100, 90]$	$[-100, 80]$
Shoulder rotation [46]	θ^r_S	$[-20, 40]$	$[-60, 95]$
Shoulder flexion	θ^f_S	$[-75, 90]$	$[-90, 130]$
Elbow flexion	θ^f_E	$[20, 140]$	$[0, 130]$
Radial pronation	θ^p	$[-90, 90]$	$[-90, 90]$
Wrist flexion	θ^f_W	$[-75, 90]$	$[-70, 70]$
Wrist abduction	θ^a_W	$[-60, 45]$	$[-10, 25]$

from shoulder abduction past 60 degrees [5], [46].
Finally the core use of the upper limb is slightly different, as macaques need to switch rapidly from powerful limb control during locomotion to fine-tuned control for fast and precise grasping [46].

Appendix B MTU functionalities

In musculoskeletal modelling was introduced the concept of moment arm to evaluate the importance of a muscle for a given motion. It is defined as the perpendicular distance from a muscle's line of action to the centre of rotation of the spanned joint, as presented in Figure B.1.

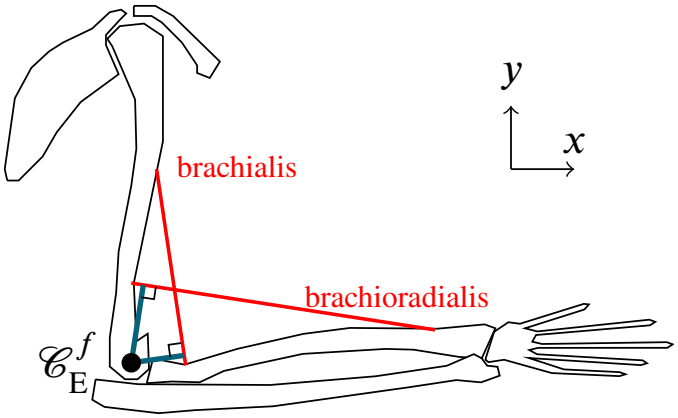

Figure B.1: The moment arm is a geometrical concept that relates to the amount of torque a muscle will be able to develop for a specific joint. Here two muscles are considered around the elbow flexion θ^f_{E}, of which the centre of rotation $\mathscr{C}^f_{\mathrm{E}}$ is shown. The elbow flexion moment arm is the shortest distance between $\mathscr{C}^f_{\mathrm{E}}$ and a muscle's line of action, and is displayed in blue for the two muscles considered.

Factually, the moment arm r_q defines how linear motion of a muscle translates into angular motion of a joint [12]. It is proportional to the moment (i.e. torque) τ_q a muscle can produce for the joint q [49]:,

$$r_q = \frac{\tau_q}{\tilde{F}}, \tag{B.1}$$

where $\tilde{F} \propto F^{MT}$ is proportional to the force vector F^{MT} produced by the MTU. Using this concept, it becomes possible to classify the MTU by their action and impact on a single DoF motion. The segregation for MTUs of the NHP model is presented in Figure B.2.

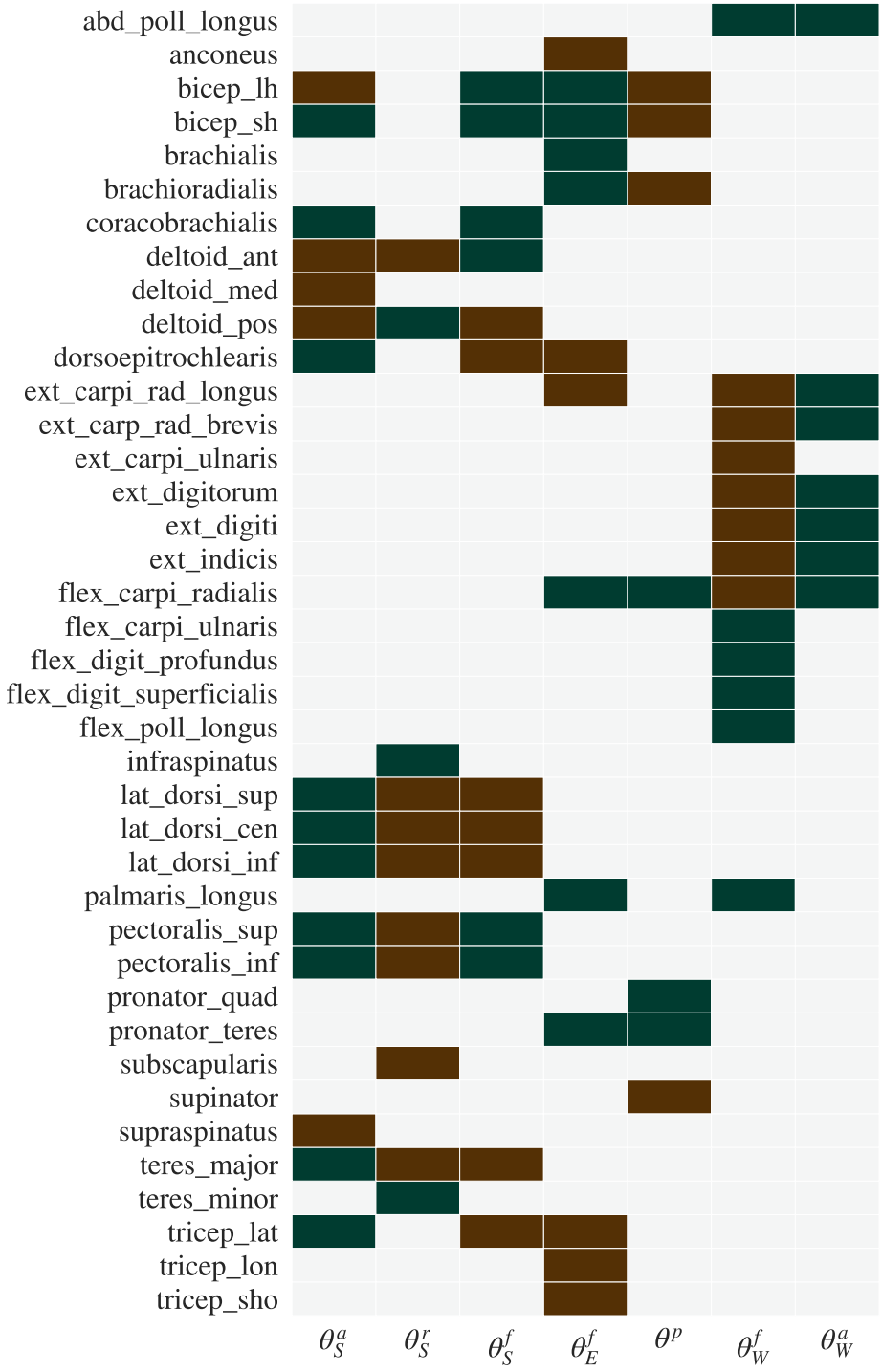

Figure B.2: MTU functions, segregated by DoF. Green indicates action in the positive sign of the angle, brown indicates the antagonist action.

Appendix C Generation of kinematics

If need be, it is possible to generate realistic marker data from the rotations parametrizing the model [5]: from a chosen joint angle evolution (i.e. elbow sigmoidal extension), the marker positions are forward-computed as follow, before being fed to the computation chain.
Around each joint the single DoF rotations are sequentially applied, defining a total joint rotation θ_S around the shoulder, θ_E around the elbow or θ_W around the wrist. The orders of rotation are:

$$\boldsymbol{\mathscr{R}}_S = \tag{C.1}$$
$$\begin{pmatrix} 1 & 0 & 0 \\ 0 & \cos(\theta_S^a) & -\sin(\theta_S^a) \\ 0 & \sin(\theta_S^a) & \cos(\theta_S^a) \end{pmatrix} \begin{pmatrix} \cos(\theta_S^r) & 0 & \sin(\theta_S^r) \\ 0 & 1 & 0 \\ -\sin(\theta_S^r) & 0 & \cos(\theta_S^r) \end{pmatrix} \begin{pmatrix} \cos(\theta_S^f) & -\sin(\theta_S^f) & 0 \\ \sin(\theta_S^f) & \cos(\theta_S^f) & 0 \\ 0 & 0 & 1 \end{pmatrix}$$

$$\boldsymbol{\mathscr{R}}_E = \begin{pmatrix} \cos(\theta_E^f) & -\sin(\theta_E^f) & 0 \\ \sin(\theta_E^f) & \cos(\theta_E^f) & 0 \\ 0 & 0 & 1 \end{pmatrix} \begin{pmatrix} \cos(\theta^p) & 0 & \sin(\theta^p) \\ 0 & 1 & 0 \\ -\sin(\theta^p) & 0 & \cos(\theta^p) \end{pmatrix} \tag{C.2}$$

$$\boldsymbol{\mathscr{R}}_W = \begin{pmatrix} 1 & 0 & 0 \\ 0 & \cos(\theta_W^f) & -\sin(\theta_W^f) \\ 0 & \sin(\theta_W^f) & \cos(\theta_W^f) \end{pmatrix} \begin{pmatrix} \cos(\theta_W^a) & -\sin(\theta_W^a) & 0 \\ \sin(\theta_W^a) & \cos(\theta_W^a) & 0 \\ 0 & 0 & 1 \end{pmatrix} \tag{C.3}$$

These rotations -evaluated in the arm state's $\mathbf{q}$- are then applied to the local position of each marker. In the following, the notation $x\big|_{humerus}$ indicates that the coordinate x is given in the local reference frame of a bone, here the humerus. This local position is invariant by definition, and each bone in the model possesses its own referential. An approximation is made for the radial pronation: it uses exactly the same centre of rotation as the elbow flexion. The marker's global position is then computed as follows, always depending on the arm segment it is attached to:

$$\vec{x}(\mathbf{q}) = \begin{cases} \boldsymbol{\mathscr{R}}_S(\mathbf{q}) \cdot \vec{x}\big|_{humerus}, & \text{for markers on the upper arm} \\ \boldsymbol{\mathscr{R}}_S(\mathbf{q})\Big(\mathscr{C}_E\big|_{humerus} + \boldsymbol{\mathscr{R}}_E(\mathbf{q}) \cdot \vec{x}\big|_{radius}\Big), & \text{— forearm} \\ \boldsymbol{\mathscr{R}}_S(\mathbf{q})\Big(\mathscr{C}_E\big|_{humerus} + \boldsymbol{\mathscr{R}}_E(\mathbf{q})\Big(\mathscr{C}_W\big|_{radius} + \boldsymbol{\mathscr{R}}_W(\mathbf{q}) \cdot \vec{x}\big|_{hand}\Big)\Big), & \text{— hand} \end{cases} \tag{C.4}$$